

Aircraft-engine particulate matter emissions from conventional
and sustainable aviation fuel combustion: comparison of
measurement techniques for mass, number, and size

Joel C. Corbin^a, Tobias Schripp^b, Bruce E. Anderson^c, Greg J.
Smallwood^a, Patrick LeClerc^q^b, Ewan C. Crosbie^{c,d}, Steven Achterberg^e,
Philip D. Whitefield^e, Richard C. Miake-Lye^f, Zhenhong Yu^f, Andrew
Freedman^f, Max Trueblood^e, David Satterfield^e, Wenyan Liu^e, Patrick
Oßwald^b, Claire Robinson^{c,d}, Michael A. Shook^c, Richard H. Moore^c and
Prem Lobo^a

^aMetrology Research Centre, National Research Council Canada, Ottawa, Ontario,
Canada

^bGerman Aerospace Center (DLR), Institute of Combustion Technology, Stuttgart,
Germany

^cNASA Langley Research Center, Hampton, Virginia, USA

^dScience Systems and Applications, Inc., Hampton Virginia, USA

^eCenter of Excellence for Aerospace Particulate Emissions Reduction Research,
Missouri University of Science and Technology, Rolla, Missouri, USA

^fAerodyne Research, Inc., Billerica, Massachusetts, USA

Correspondence to: Joel C. Corbin (Joel.Corbin@nrc-cnrc.gc.ca) and Prem Lobo
(Prem.Lobo@nrc-cnrc.gc.ca)

0 AMT Feature: short summary (max. 500 characters incl. spaces)

The combustion of sustainable aviation fuels in aircraft engines produces particulate matter (PM) emissions with different properties than conventional fuels due to changes in fuel composition. Consequently, the response of various diagnostic instruments to PM emissions may be impacted. We found no significant instrument biases in terms of particle mass, number, and size measurements for conventional and sustainable aviation fuel blends despite large differences in the magnitude of emissions.

1 Abstract

Sustainable aviation fuels (SAFs) have different compositions compared to conventional petroleum jet fuels, particularly in terms of fuel sulphur and hydrocarbon content. These differences may change the amount and physicochemical properties of volatile and non-volatile particulate matter (nvPM) emitted by aircraft engines. In this study, we evaluate whether comparable nvPM measurement techniques respond similarly to nvPM produced by three blends of SAFs compared to three conventional fuels. Multiple SAF blends and conventional (Jet A-1) jet fuels were combusted in a V2527-A5 engine, while an additional conventional fuel (JP-8) was combusted in a CFM56-2C1 engine.

We evaluated nvPM mass concentration measured by three real-time measurement techniques: photoacoustic spectroscopy, laser-induced incandescence, and the extinction-minus-scattering technique. Various commercial instruments were tested including three LII 300s, one PAX, one MSS+, and two CAPS PM_{SSA}s. Mass-based emission indices (EI_m) reported by these techniques were similar, falling within 30% of their geometric mean for EI_m above 100 mg/kg_{fuel} (approximately 10 $\mu\text{g PM m}^{-3}$ at the instrument), this geometric mean was therefore used as a reference value. Additionally, two integrative measurement techniques were evaluated: filter photometry and particle size distribution (PSD) integration. The commercial instruments used were one TAP, one PSAP, and two SMPSs. These techniques are used in specific applications, such as on-board research aircraft to determine PM emissions at cruise. EI_m reported by the alternative techniques fell within approximately 50 % of the mean aerosol-

52 phase EI_m .

53 In addition, we measured PM-number-based emission indices using PSDs and
54 condensation particle counters. The commercial instruments used included TSI
55 SMPSs, a Cambustion DMS500, and an AVL APC, and the data also fell within
56 approximately 50 % of their geometric mean. The number-based emission indices
57 were highly sensitive to the accuracy of the sampling-line penetration functions
58 applied as corrections. In contrast, the EI_m data were less sensitive to those
59 corrections since a smaller volume fraction fell within the size range where
60 corrections were substantial. A separate, dedicated experiment also showed that
61 the operating laser fluence used in the LII 300 laser-induced incandescence
62 instrument for aircraft engine nvPM measurement is adequate for a range of SAF
63 blends investigated in this study. Overall, we conclude that all tested instruments
64 are suitable for the measurement of nvPM emissions from the combustion of SAF
65 blends in aircraft engines.

66 Keywords: non-volatile particulate matter, aircraft, emissions, sustainable
67 aviation fuels, black carbon

68 2 Introduction

69 Aircraft engine particulate matter (PM) emissions are composed of non-volatile
70 (black carbon, metal ash, oxygenated functional groups) and volatile components
71 (volatile organic compounds, nitrates, sulphates) (Gagné et al., 2021; Masiol and
72 Harrison, 2014; Petzold et al., 2011). The non-volatile particulate matter (nvPM)
73 emissions are formed in the combustor, while volatile particulate matter (vPM)
74 emissions, present in the gas phase at the engine exit, condense after emission.
75 Aircraft engines emit vPM with similar or greater orders of magnitude as nvPM,
76 especially after the vapour pressure of volatile species is lowered by oxidative
77 aging (Kiliç et al., 2018) or by cooling (Beyersdorf et al., 2014). The nvPM and vPM
78 are constituents of total PM which affects air quality, health, and climate. The
79 International Civil Aviation Organization (ICAO) has developed standards and
80 recommended practices (SARPs) for measuring the mass- and number-based
81 emissions of nvPM emitted from aircraft engines with maximum rated thrust >26.7
82 kN (ICAO, 2017). Currently, SARPs have not been established for vPM or total PM

(Lobo et al., 2020). The SARPs for nvPM specify standardized sampling and measurement protocols (SAE, 2013, 2018; ICAO, 2017), which have been extensively evaluated and validated (Lobo et al., 2015b, 2020; Kinsey et al., 2021). The nvPM regulatory limits are applicable for type certification of aircraft engines, but they do not address the vPM which may have substantial environmental impacts.

To reduce CO₂ emissions, mitigate environmental impacts, and make the aviation sector more sustainable, a significant effort is underway to develop and deploy sustainable aviation fuels (SAFs). Various feedstocks and different conversion pathways can be used to produce SAFs (Hileman and Stratton, 2014), which differ in chemical and physical properties compared to conventional petroleum jet fuel (Vozka et al., 2019), most notably by lacking aromatic and sulfur species that are precursors to nvPM and vPM emissions. New SAF candidates must undergo a rigorous qualification and approval process (ASTM D4054) prior to being certified under the ASTM D7566 standard specification as a blending component. Currently, the ASTM D7566 standard allows SAF blend ratios of up to 50% with conventional fuel for drop-in fuels (Wilson et al., 2013).

The combustion of neat SAFs and blends with conventional jet fuel has been shown to result in different PM emissions characteristics as a function of engine type and operating condition (Beyersdorf et al., 2014; Brem et al., 2015; Corporan et al., 2011; Lobo et al., 2011, 2015a, 2016; Moore et al., 2017; Schripp et al., 2018, 2019; Timko et al., 2010). In addition to changes in PM mass- and number-based emissions, SAF combustion results in changes to particle size distributions (PSD) (Beyersdorf et al., 2014; Cain et al., 2013; Kinsey et al., 2012; Lobo et al., 2011, 2015a, 2016; Schripp et al., 2018; Timko et al., 2010), chemical composition (Elser et al., 2019; Kinsey et al., 2012; Timko et al., 2013; Williams et al., 2012), morphology (Huang and Vander Wal, 2013; Kumal et al., 2020; Liati et al., 2019), hygroscopic properties (Trueblood et al., 2018), and optical properties (Elser et al., 2019).

115 The standardized sampling and measurement protocol for aircraft engine nvPM
116 emissions was designed and validated for engine certification tests using
117 conventional jet fuel. The SARPs require that number-based nvPM emissions are
118 measured with a butanol-based condensation-nuclei counter with a 50% cut-off
119 size of, at most, 10 nm sampling in single-particle-counting mode downstream of a
120 diluter and catalytic stripper. For mass-based nvPM emissions, the instrument
121 must be insensitive to vPM and able to meet performance specifications for
122 repeatability, zero drift, linearity, limit of detection, rise time, sampling interval,
123 accuracy, and applicability. Limited information is available on aircraft engine
124 nvPM emissions characteristics measured with the standardized system for
125 different engine types burning SAFs and blends with conventional fuel (Durand et
126 al., 2021; Elser et al., 2019; Lobo et al., 2015a, 2016).

127
128 The standardized system components are not easily adaptable for use on aircraft
129 for measurement of cruise level nvPM emissions. Consequently, there are no
130 comparable in-flight engine-emissions data available for developing and validating
131 models that predict cruise nvPM-emissions based on engine certification data.
132 Particle size distribution measurements are also not included in the standardized
133 system, which are important for assessing the effects of fuels, operating conditions,
134 and engine technologies on the environmental impacts of PM emissions. Thus to
135 advance our understanding of aircraft engine emissions and the factors that
136 control them as well as to develop a large and consistent observational data base,
137 it is important to evaluate the relative performance of other diagnostic
138 instruments that are not prescribed in the standardized protocol but meet these
139 needs. Such instruments must be evaluated for their response to nvPM and total
140 PM emissions from aircraft engines using standardized and non-standardized
141 systems, and for measurements at the engine exit plane and downstream of the
142 engine in the near field, since these instruments are typically used with minimal
143 change to their operating parameters for a wide range of sampling conditions. Very
144 limited data are available in the literature for this purpose, and no data have yet
145 been published for SAFs.

146

Here, we present the inter-comparison of real-time measurements of aircraft engine nvPM emissions in terms of physical characteristics such as mass, number, and size distributions using different diagnostic instruments and measurement principles. The nvPM mass emissions were evaluated using three real-time measurement techniques: photoacoustic spectroscopy, the extinction-minus-scattering technique, and laser-induced incandescence (LII), and two alternative measurement techniques widely used in laboratories and on-board aircraft: filter-based photometry and PSD integration. We note that one of the photoacoustic instruments and the LII instruments have been demonstrated to be compliant with the ICAO SARPs performance specifications. The PM number-based emissions were measured using a condensation particle counter. The PSD characteristics measured by scanning mobility particle sizers and an electrical mobility spectrometer were also compared. The nvPM and total PM emissions were delineated using a thermal denuder and a catalytic stripper. We also report the effect of laser fluence on the laser-induced incandescence of nvPM for SAF combustion as changing carbon nanostructure is known to influence particle light absorption and consequently LII signals, and hence the derived nvPM mass concentration. The impact of fuel composition on PM emissions will be reported separately (Schripp et al., 2022).

3 Methods

The observations presented in this paper were collected during the NASA/DLR-Multidisciplinary Airborne Experiment (ND-MAX)/ Emission and Climate Impact of Alternative Fuel (ECLIF) 2 campaign that was conducted at Ramstein Air Base, Ramstein-Miesenbach, Germany in January-February 2018. The campaign included ground-based and in-flight measurements of emissions from the DLR Advanced Technology Research Aircraft (ATRA) A320 aircraft with V2527-A5 engines running on two conventional jet fuels and three blends with SAF. The main objective of the ground-based measurements was to characterize the nvPM, total PM, and hydrocarbon emissions as functions of engine thrust condition and fuel composition. Several identical instruments were included in the in-flight sampling aircraft (NASA DC-8) and ground measurement diagnostic instrument suites to enable comparisons of engine emissions during ground and airborne operations,

and create a data set for testing cruise emission models. The NASA DC-8 aircraft with CFM56-2C1 engines was also used as an emissions source to compare various emissions diagnostic instruments during the ground-based measurements.

3.1 Engine and fuels

In the majority of this work, emissions were sampled from a single IAE mixed-flow V2527-A5 starboard engine of the DLR ATRA aircraft (Airbus A320-232). The engine was operated on two conventional, petroleum jet fuels, referred to as REF3 and REF4, and three sustainable aviation fuel blends, referred to as SAF1, SAF2, and SAF3. The abbreviations for the two conventional petroleum fuels are used to avoid confusion with the previous ECLIF campaign (Schripp et al., 2018).

A limited number of experiments were also performed with JP-8 fuel, combusted in the starboard CFM56-2C1 engine (#3) of the NASA DC-8 aircraft. Due to limited fuel availability, none of the other five fuels could be combusted in the CFM56-2C1 engine. The properties of the six fuels are summarized in Table 1.

3.2 Ambient conditions

The measurements presented here were performed outdoors during winter in western Germany. Detailed meteorology for each test point is given in the supplement. The minimum, median, and maximum temperatures were 2.3, 2.9, 8.3 °C, respectively. Conditions were humid (>83 % humidity) and sometimes rainy. Winds ranged from 0 to 15.5 km h⁻¹ and wind direction was sometimes variable. The median wind direction was south-westerly, while the source aircraft was oriented facing to the east. Consequently, winds blowing approximately 45° angle from the right rear of the source aircraft sometimes prevented the engine emissions from reaching the sampling probe at low engine thrust settings.

3.3 Emissions sampling

An extensive suite of aerosol and gas-phase instruments operated by the members of six different institutions were deployed in two different shipping

209 containers to characterize the emissions (Table 2). The complete emission-
210 sampling setup is discussed in a companion paper (Schripp et al., 2022). Briefly,
211 emissions were sampled through a probe located 43 m downstream of the
212 starboard engine of the aircraft. The probe was placed in front of a blast fence
213 located on the western side of the Ramstein Air Force Base flight line, and the fence
214 redirected the engine exhaust upwards for safety. The probe was connected to a
215 18.5-mm ID, 20-m-long electrically-conductive sampling line heated to 60 °C, that
216 transported flow to a sampling plenum maintained at 33 °C. To minimize residence
217 time and particle losses in this sampling line, a pump ensured that a total of at least
218 137 L min⁻¹ flowed through the sampling manifold at all times. Higher flows
219 produce an unacceptably large pressure drop in the primary sampling line. The
220 majority of this flow was discarded as excess.

221
222 The plenum was placed inside a modified shipping container (Container 1) behind
223 the blast fence, along with the NRC, DLR, and NASA instruments. The North
224 American Reference System (NARS) was connected to the plenum by a short
225 section of heated line to the NARS dilutor box, which was heated to 60 ± 15 °C and
226 contained a custom Dekati dilutor with a dilution factor of approximately 4 (less
227 than the standard Dekati dilutor factor of 8 to 14). A 25 m line heated to 60 ± 15 °C
228 transferred sample aerosols flow from the dilutor box to a second shipping
229 container (Container 2), where the MST and ARI instruments were connected. The
230 NARS components include the 25 m heated line, attached diluters and MST
231 instrument suite; the system is compliant with specifications for the standardized
232 nvPM sampling and measurement system (SAE, 2013; SAE, 2018; ICAO, 2017) and
233 whose performance has been demonstrated and evaluated in previous studies
234 (Lobo et al., 2015b, 2016, 2020). Additional instrumentation installed as part of
235 the NARS included a fast electrical mobility spectrometer (Cambustion DMS500),
236 an Aerodyne Aerosol Mass Spectrometer (results not presented here), and a CAPS
237 PM_{ss} monitor (Aerodyne Research Inc.). The details of the instruments installed
238 inside these two containers are listed in Table 3.

3.3.1 Gaseous measurements

A suite of gaseous emissions was measured in this study, as summarized in Table 2. The CO₂ measurements from the NASA LI-COR 7000 were in good agreement with those taken by DLR (MKS MultiGas 2030 FTIR Continuous Gas Analyzer) and MST (LI-COR model 840A), but had a faster response time and were therefore used as the reference for instruments in Container 1. Instruments in Container 2 used the MST measurements as reference.

3.3.2 nvPM number and particle size distributions (PSDs)

nvPM number concentration was measured directly by a certification-test-compliant, particle counter, APC (AVL Inc., which contains a TSI Model 3790E CPC), which was part of the NARS in Container 2. PSDs were measured with two technologies: scanning mobility particle sizers (SMPS, TSI Inc.) and electrical mobility sizers (EMS). Two types of EMS were used; the Cambustion DMS500 (in Container 2, measuring particles 5 to 1000 nm in diameter; data processed with a bimodal calibration matrix and log-normal inversion) and the TSI Engine Exhaust Particle Sizer (EEPS, Container 1, measuring particles from 6 to 523 nm). However, the EEPS data were excluded from this analysis due to unidentified problems with the instrument which led to anomalous PSDs.

Two SMPSs measured nvPM PSDs. An SMPS operated by NRC measured particles 10 to 278 nm in diameter downstream of a catalytic stripper (Model CS015, Catalytic Instruments GmbH), which heated samples to 350 °C before oxidizing gas-phase VOCs to prevent them from recondensing after exiting the device. Another SMPS operated by NASA measured particles 10 to 278 nm in diameter either directly or downstream of a NASA-constructed thermal denuder (TD) also operated at 350 °C. The TD employs a concentric activated charcoal filter downstream of the sample heater to prevent re-condensation of volatile species. TDs are commonly used on-board aircraft for measuring nvPM number concentration and size distributions (Clarke, 1991; Moore et al., 2017) and have been shown to effectively evaporate nucleation and accumulation mode sulfate and organic aerosols (Beyersdorf et al., 2014; Schripp et al., 2018).

3.3.3 nvPM mass measurements

In this study, most of the nvPM mass data were derived from light absorption coefficients (units of m^{-1}), either determined in flow-through sample cells (the CAPS PM_{SSA} , PAX, and MSS introduced below) or after collecting particles onto a filter (the TAP and PSAP introduced below). Such absorption measurements can be converted to equivalent black carbon or eBC mass concentrations (eBC, units of g m^{-3} ; Petzold et al. (2013)) by dividing them by a reference mass absorption cross-section (MAC, units of $\text{m}^2 \text{g}^{-1}$). The LII measurements also rely on light absorption, although the measurand is not absorption but incandescence at two wavelengths and is termed rBC (Petzold et al., 2013; Michelsen et al., 2014).

The reference MAC used to report eBC represents an assumed physical property of the nvPM emitted by the engine at a given time. The extensive review of Bond and Bergstrom (2006) concluded that the MAC at 550 nm of externally-mixed BC from a variety of sources could be summarized as $7.5 \pm 1.2 \text{ m}^2 \text{g}^{-1}$; the more recent review of in-situ measurements by (Liu et al., 2020) recommended $8.0 \pm 0.7 \text{ m}^2 \text{g}^{-1}$ at 550 nm. In this study, we have used the Bond and Bergstrom value of $7.5 \text{ m}^2 \text{g}^{-1}$ for consistency with earlier work and instrument software. These values are assumed to vary inversely with wavelength, with an Angstrom (power) exponent of 1; for example, the 660 nm CAPS PM_{SSA} monitor data were processed with a MAC of $7.5 \text{ m}^2 \text{g}^{-1} \times (550 \text{ nm} / 660 \text{ nm})^1 = 6.5 \text{ m}^2 \text{g}^{-1}$.

One eBC technique, the CAPS PM_{SSA} monitor (Aerodyne Research Inc.; Onasch et al., 2015) derives absorption coefficients as the difference between measured aerosol extinction and scattering coefficients, from which eBC concentrations were calculated as described above. The CAPS PM_{SSA} measures light extinction by the calibration-free cavity attenuation phase shift (CAPS) technique and light scattering with an integrating nephelometer. The CAPS technique measures the lifetime of photons in a high-finesse optical cavity comprised of two high reflectivity mirrors, from which the extinction coefficient can be calculated. An integrating nephelometer captures light scattered from a section of this cavity, and is calibrated using the measured extinction of small (Rayleigh regime) non-absorbing particles. In this study, two CAPS PM_{SSA} monitors were present, one operated at 630 nm wavelength by ARI and the other at 660 nm wavelength by

301 NRC. The scattering channel of the NRC CAPS PM_{SSA} was calibrated on-site using
302 nebulized and dried ammonium sulfate particles; the other instruments were
303 similarly calibrated prior to the campaign at the manufacturer using 200 nm
304 ammonium sulfate. For the sub-200 nm particles measured in this study, no
305 truncation corrections (Modini et al., 2021) were necessary.

306 Two other eBC instruments were based on photoacoustic spectroscopy, namely
307 the Photoacoustic Extinctionmeter (PAX, DMT Inc., Nakayama et al., 2015) and the
308 Micro Soot Sensor (MSS; AVL GmbH; Schindler et al., 2004). In both of these
309 instruments, aerosol absorption is measured by the periodic heating of particles
310 using a modulated laser, resulting in the generation of pressure waves which are
311 amplified by an acoustic cell and detected by a microphone. The PAX was
312 calibrated using nebulized ammonium sulfate as well as graphitic nanoparticles
313 (Aquadag).

314 During on-site calibration of the PAX using graphitic Aquadag nanoparticles, the
315 PAX signals were observed to drift slowly upwards after each baseline. We were
316 nevertheless able to obtain useful data by configuring the PAX to auto-baseline
317 every 180 seconds, and only using the first 15 seconds of measurements after each
318 baseline. After the campaign, it was found that a component of the circuit board
319 was damaged during the initial shipment. In spite of this electrical problem, the
320 PAX data do not represent outliers in the following analysis.

321 Two additional pairs of eBC instruments were deployed at the ground site and on-
322 board the NASA DC-8 that measured aerosol absorption coefficients based on filter
323 attenuation, namely a Particle Soot Absorption Photometer (PSAP, Radiance
324 Research; Bond et al., 1999) and Tricolor Absorption Photometer (TAP, Brechtel
325 Manufacturing Inc., ; Ogren et al., 2017). These instruments were designed as low-
326 cost, low-maintenance devices for monitoring aerosol optical properties in the
327 background atmosphere (i.e., at low concentrations) and have been used
328 previously in airborne and ground-based studies (Moore et al., 2017). In these
329 instruments, particles are continuously collected onto an internal filter while its
330 light attenuation is measured. The change in light attenuation over time is used to
331 calculate absorption coefficients. This calculation requires post-processing to

332 correct for filter loading effects (which do not require independent measurements)
333 and may also be corrected for light attenuation due to scattering rather than
334 absorption (which requires an independent nephelometer measurement)
335 (Virkkula, 2010). Other sources of error include nonlinearities due to size-
336 dependent penetration of particles into the filter media and the evaporation of
337 volatile species over time (Lack et al., 2014; Nakayama et al., 2010). We note that
338 the TAP automatically advances its filter when its transmission drops below 80%,
339 whereas the PSAP requires a manual filter change. The PSAP filter was therefore
340 changed manually before each set of experiments herein, to ensure that its filter
341 transmission remained above 80% during all measurements.

342 Three Artium LII 300 (Artium Technologies) instruments measured rBC, based on
343 two-colour pulsed laser-induced incandescence (LII) (Snelling et al., 2005). These
344 instruments heat nvPM using a 1064 nm pulsed laser and measure the resulting
345 incandescence at two wavelength bands. From this measurement, rBC temperature
346 and mass concentrations can be calculated. One of the LII 300s was a component of
347 the NARS. Of the other two, one was dedicated to an experiment where its
348 operating conditions were varied (Section 4.6). Therefore, only two LII 300s were
349 measuring real-time nvPM mass concentration simultaneously at any given time.
350 The MSS+ and the LII 300s were calibrated by reference to the elemental carbon
351 mass (defined by thermal-optical analysis) produced by a laboratory diffusion-
352 flame combustion aerosol source using measurements at three mass
353 concentrations spanning 0.1 to 0.5 mg m⁻³ (SAE, 2018).

354 Finally, the SMPS PSDs were converted to equivalent mass concentrations by the
355 integrated PSD approach, described in detail by Momenimovahed and Olfert
356 (2015). In brief, the equivalent mass of each SMPS-reported mobility diameter was
357 calculated using an effective density of 1000 kg m⁻³, which has been shown to
358 produce better than 20% accuracy relative to more complete, size-resolved
359 effective densities (Durdina et al., 2014).

360 3.4 Data analysis

361 3.4.1 Emission index calculations

362 The raw data were analysed over comparable time intervals and cross-
363 checked by independent calculations. The general analysis proceeded as described
364 in this section. First, the time series of measured CO₂ concentrations was used as a
365 reference against which to synchronize all time series, based on rapid rises and
366 falls in the observed concentrations (measured at 1 Hz) when the engine thrust
367 condition underwent large changes (as shown at 08:00 in Figure 2). All
368 instruments were synchronized against the NASA CO₂ sensor except the
369 instruments in container 2, which was synchronized against the MST LI-COR CO₂
370 sensor, because of the additional dilution stage. The time synchronization
371 accounted for different lag times due to differences in the response times and clock
372 accuracy of each instrument.

373 Second, the CO₂ concentrations [CO₂] were baseline-subtracted and filtered as
374 follows. The CO₂ baseline ([CO₂]_b) was calculated as the mean of the CO₂
375 concentrations measured before ([CO₂]₀) and after ([CO₂]₁) each test. The
376 uncertainty in this baseline value was calculated as either ([CO₂]_b – [CO₂]₀) or
377 ([CO₂]_b – [CO₂]₁), whichever was greater.

378 Due to the prevailing crosswind mentioned above, unstable CO₂ concentrations
379 occurred during some test points at the idle engine thrust condition. These
380 unstable conditions were identified and filtered using two separate methods. In
381 the first method, the SMPS PSDs were inspected for reproducibility. In the second
382 method, an algorithm was used to reject any test points with CO₂ uncertainties
383 greater than 50%, CO₂ signals less than a factor of ten greater than uncertainty, or
384 CO₂ signals less than 20% above baseline. We found that the first method rejected
385 all of the points rejected by the algorithm, in addition to a few additional points.
386 The analysis presented uses the first method.

387 Third, all data were arithmetically averaged over the test point periods defined in
388 Table S1. For each instrument, the averaging periods were refined by inspection of
389 the data since sampling-line residence times varied. The averaged data were

typically at 1 Hz sampling frequency initially, although the SMPS instruments measured PSDs at 45 second intervals (NRC instrument) or 30 second intervals (NASA). Emission indices (EIs) were then calculated from the averaged data following (SAE, 2013):

$$EI_m = PM_m \frac{RT_m}{[CO_2](M_c + \alpha M_H)P_m} \quad (1)$$

$$EI_{num} = PN \times 10^6 \frac{RT_m}{[CO_2](M_c + \alpha M_H)P_m} \quad (2)$$

Where EI_m and EI_{num} are mass and number-based EIs, respectively; PM_m and PN are mass and number concentrations, respectively, at standard reference temperature (T_m ; 273.15 K) and pressure (P_m ; 1 atm); α is the hydrogen to carbon ratio of the fuel; M_c and M_H are the molar masses of carbon and hydrogen, respectively; and R is the ideal gas constant (0.082 L.atm.K⁻¹.mol⁻¹).

3.4.2 Penetration correction

Particles may be lost to the walls of sampling lines or to deposits on those walls. The fraction of particles penetrating a given system varies with size, according to a characteristic penetration function. Four penetration functions were applied in this study: 1) from the probe to the sampling plenum, 2) from the plenum to the NARS, 3) within the TD, and 4) within the CS (Figure 4). Function 1 was measured on site as described below. Function 2 was calculated using the standard equations for line penetration, as detailed in the loss calculation methodologies provided in SAE documents AIR6504 (SAE, 2017) and ARP6481 (SAE, 2019). Function 3 was experimentally determined in the laboratory by NASA. Function 4 was obtained from theoretical estimates and experimental measurements (Catalytic Stripper manual, 2014).

Penetration function 1 (probe-to-plenum penetration) was measured experimentally by nebulizing ammonium sulfate particles at the probe while all instruments were sampling and all heated lines had reached thermal equilibrium. (Function 1 therefore also includes the smaller instrument sampling lines

downstream of the plenum in its correction as well; however, these were considered negligible relative to the longer probe-to-plenum and plenum-to-Container-2 transport lengths.) For this measurement, the NRC SMPS was moved to the probe, while the NASA instrument remained in its standard position. The ratio of the NASA to NRC PSDs (GMD 30 nm, GSD 1.7) then provided a first estimate of the penetration function. However, this first estimate was not accurate, as the measurements were performed on a cold day (measured as approximately 5 °C outdoors and 15 °C in the instrument container) and as it does not account for performance differences between the NASA and NRC SMPSs. Therefore, two corrections were made. First, both measurements were corrected to standard temperature and pressure. Second, differences between the two instruments were directly measured by moving the NRC SMPS just outside of the sampling container (to keep it at 5 °C) and connecting it to an identical sampling line as the NASA SMPS. The ratio of the two measured PSDs in this setup was defined as equal to unity at all sizes, and used to correct the initial penetration function. Therefore, no further correction was made for sampling lines in Container 1. Losses in this additional line were negligible (calculated penetrations of 0.997 at 100 nm and 0.98 at 20 nm) relative to the long NARS line to Container 2 (i.e., Function 2).

All reported data are corrected for these penetration functions. Size-resolved data (SMPS) were corrected using the size-resolved penetration functions shown in Figure 4. Size-integrated data (all other instruments) were corrected by weighting the penetration functions by the corresponding measured SMPS PVDs. The correction factors are given in the Data Availability section.

3.5 Uncertainties

All reported uncertainties and error bars represent standard errors, propagated through the calculation as necessary. When two independent sources of uncertainty were available (for example, the standard error in the 10 second averages of [CO₂] and the uncertainty in the baseline value) they were added in quadrature. Our bottom-up calculations of uncertainty can be compared with the spread of the data points in our EI comparisons below. This spread represents a

top-down uncertainty, and is similar in magnitude to the bottom-up uncertainties (i.e. error bars). This similarity lends confidence to our uncertainty estimates. In most figures, error bars have generally been omitted for clarity, but uncertainties are given for each instrument at each test point in Table S1.

4 Results and discussion

4.1 Experiment overview

A typical time series obtained when the emissions from the IAE V2527-A5 engine were sampled is shown in Figure 2. Nominal low-pressure turbine fan speeds (N1) expressed as a percentage of maximum continuous thrust, are shown by the labels at the top of the figure. Percent N1 (along with engine fuel flow rate) is another metric for representing the different engine thrust conditions and is used as a primary independent variable in this study. The CO₂ concentrations (red line) were highly variable at N1 = 23% as the ambient wind shifted the aircraft exhaust plume toward and away from the sampling probe. Correspondingly, both nvPM mass and PSD measurements were highly variable, as shown by the blue trace and black symbols, respectively.

As shown in Figure 3a, nvPM mass concentrations, represented by El_m , increased with increasing N1 before decreasing slightly at the highest N1, similar to the trends for other engine types reported by Lobo et al. (2015b, 2020). Figure 3b shows that the relationship for El_{num} is less clear, with a slight increase at moderate N1 followed by a greater decrease at high N1. As discussed below (Section 4.2.3), the higher El_m at higher N1 thrust was associated with larger particle sizes, and therefore smaller penetration-function corrections (Section 4.2.1). Finally, for context, Figure 3c shows the relationship of the PM mass concentrations, used to calculate El_m (based on the geometric mean El_m discussed in Section 4.4.1), with baseline-subtracted CO₂ concentrations from the measured plume. An effect of fuel composition is evident, and discussed in detail in Schripp et al., (2022).

4.2 Size distributions and penetration functions

4.2.1 Penetration function

A typical PSD, and corresponding PVD, are shown in Figure 4, in the context of the penetration functions applied in this work. The PVD was calculated by assuming spherical particles, which incurs negligible error for aircraft-engine nvPM due to the small diameter of particles produced by such engines (Durdina et al., 2014; Saffaripour et al., 2020). For the example PSD and PVD in Figure 4 (shading), it is clear that a substantial fraction of the particle number was corrected for penetrations (lines) of roughly 0.5. In contrast, the larger mode of the PVD corresponds to penetrations larger than 0.8 in most cases. These differences led to a median number- and mass-based correction factors of 1.51 and 1.19, respectively for penetration Function 1 (probe to plenum) labelled in the figure. The remaining instrument-specific penetration corrections were applied according to the position of each instrument in the sampling system, as specified in Table 2. The magnitude of each correction is given in Table S1.

4.2.2 PSDs

Figure 5 shows selected PSDs from the IAE V2527-A5 engine operated with SAJF1 (Figure 5a) and REF4 (Figure 5b) fuels. The PSDs are corrected for line penetration as described above. The plot illustrates a lower (40 % N1) and a higher thrust point (60 % N1) from the available data for two fuels. Note that the ordinate scales are harmonized across the upper and lower rows only. All abscissa scales are harmonized. The figure indicates roughly comparable PSDs from these two fuels. The companion paper (Schripp et al., 2022) compares the effects of fuel composition in detail.

The CFM56-2C1 engine on the DC-8 burning JP-8 emitted an order of magnitude more total particles per unit fuel burned than any of the fuels combusted in the ATRA (data not shown). We attribute this difference to the relatively high sulfur content of the JP-8 fuel (1490 ppm sulfur versus ≤ 105 ppm for the other fuels). The CFM56-2C1 engine also emitted a factor of three lower nvPM mass and nvPM number than the V2527-A5 engine.

510 The presence of extremely small particles with $d_m < 10\text{nm}$ was evident in the two
511 nvPM PSDs (not shown due to the extremely large penetration function at these
512 sizes; Figure 4). The CS-SMPS data extended to smaller diameters, and showed that
513 the size range measured by these two instruments was insufficient to capture the
514 full PSD for the CFM56-2C1 engine data at 22% N1 as well as 63% N1. The $d_m <$
515 10nm mode was not as prominent in the V2527-A5 engine exhaust at any thrust,
516 although some evidence was observed for it (e.g. number distribution at 40% N1 in
517 Figure 5b). Our data do not allow us to identify whether these small particles were
518 non-volatile or represent an imperfect performance of the CS and TD.

519
520 There is some evidence for an increase in SMPS-calculated volume at larger
521 particle sizes in Figure 5a, at both 40% and 60% N1. If these large particles
522 indicated the presence of a large aerosol mode which varied independently from
523 the primary mode (e.g. if they were emitted by some other process than the engine
524 itself), they would introduce a EI_m -dependent bias in the ratio of SMPS-based EI_m
525 to other instruments, which was not observed (Section 4.4.2).

526
527 Since the CFM56-2C1-with-JP-8 data were strongly influenced by a nucleation
528 mode, and were therefore not well described by the GMD and GSD of the data,
529 these measurements have been omitted from all subsequent PSD analysis in this
530 manuscript. Bimodal fits to the data were not possible as the nucleation mode was
531 not captured by our size distributions. However, the nvPM mass measurements
532 are much less sensitive to these small particles (Hinds, 1999) and have therefore
533 been retained. PSDs from all instruments, test points, and fuels from both the
534 CFM56-2C1 and V2527-A5 engines are included in the supplement.

535 4.2.3 Particle size statistics; GMD and GSD

536 Figure 6 summarizes the PSDs measured by three instruments in terms of their
537 GMD and GSD. The data sets labelled SMPS and TD-SMPS were both obtained from
538 NASA's SMPS, which was manually switched to a bypass line and the TD at each
539 test point. The data set labelled CS-SMPS was obtained with NRC's SMPS.

540 Total PM is represented by the data sets labelled DMS500 and SMPS. However, the
541 two are not directly comparable because the DMS500 measurements were
542 obtained after an additional dilution by a factor of 4 in the NARS and the DMS500
543 was not operated behind a volatile particle remover (CS or TD). Moreover, the
544 inversion of DMS500 data requires more assumptions about the particle size
545 distribution than the analogous SMPS calculation. Either volatiles or this inversion
546 procedure may have caused the 10% larger GSDs observed for the DMS500 for
547 some data (some measurements with GMDs over 35 nm) relative to the SMPS.
548 Since volatiles would affect both GMD and GSD, but we primarily observed
549 discrepancies in the DMS500 GSD, we suggest that the inversion was the major
550 source of bias in these data.

551
552 nvPM is represented by the open circles and filled squares in Figure 6. These two
553 data sets show a different relationship (slope) between GMD and GSD, reflecting
554 systematic differences in the corresponding PSDs. Relative to the mean of the two
555 instruments, the NRC GMDs were higher (Figure 7a) while the NRC GSDs were
556 higher at $GSD < 1.75$ but lower at $GSD > 1.75$ (Figure 7b). Inspection of the
557 corresponding PSDs showed that the NASA and NRC instruments agreed at higher
558 d_m but that NRC number concentrations were higher at smaller d_m . This trend
559 suggests that a bias in the penetration functions applied to each instrument
560 (Figure 4, Table 2) led to the discrepancy in GMD and GSD. Such a bias would affect
561 the nvPM concentration estimated from these PSDs (Figure 8b) and will be
562 discussed further below.

563 In spite of these trends in GMD and GSD, the PSD measurements agreed to within
564 20% (Figure 7a) for nvPM GMDs and within 5% for nvPM GSDs (Figure 7b).
565 Furthermore, these measurements are consistent with previous measurements by
566 Lobo et al. (2015c), as illustrated by the line in Figure 6, which reproduces the
567 polynomial best-fit line reported by those authors.

4.3 Consistency between number-based emission indices of nvPM and vPM

Figure 7c compares the measured vPM and nvPM El_{num} with the mean nvPM El_{num} (i.e., mean of the NRC CS-SMPS, NASA TD-SMPS, and NARS APC. The grey shading shows that all instruments agreed to within a factor of 2. The APC and DMS500 nvPM El_{num} were both typically higher than the two similar SMPSs. Substantial variability between the two SMPSs was also observed.

In Figure 7c, the penetration-corrected APC El_{num} are approximately 50% larger than the SMPS El_{num} under all conditions. Our measured PSDs rule out the possibility that 50% of particles were not seen by the SMPS. Therefore, we attribute the difference between APC and SMPS results to uncertainties in the APC or SMPS penetration correction functions (Figure 4), i.e., we hypothesize that this difference would not have been observed had the instruments all sampled from the same plenum from comparable sampling lines.

We also attribute the larger nvPM El_{num} measured by the DMS500 to the same cause; to which a similar penetration function as the APC applies (Section 3.4.2). We note that the DMS500 measured total PN, not nvPN, so is expected to report higher number concentrations when volatile particles are present.

4.4 Consistency between mass-based emission indices

4.4.1 El_m measurements by real-time sampling instruments

Figure 8a presents scatterplots of the real-time El_m measurements acquired during this study for all fuels and both engine types. In Figure 8a, the individual El_m are plotted against the geometric mean of the instruments shown in the caption: three LII 300 instruments, two CAPS instruments, one PAX and one MSS+. The geometric mean was chosen over the more-common arithmetic mean because the data are not normally distributed; the arithmetic mean would therefore have over-emphasized outliers.

Figure 9a presents the same data as Figure 8a except that the ordinate data have

597 been normalized to the geometric-mean El_m from Figure 8a. Most data fall within
598 30 % of the mean (inner dashed lines) above 100 mg / kg_{fuel}. We note that exhaust
599 samples were diluted with background air by a factor of 40 or more before
600 reaching the inlet probe, so at this lower limit, the actual concentration observed
601 by the instruments was approximately 10 $\mu\text{g m}^{-3}$ (the exact conversion factor
602 varies with CO₂ concentration and fuel properties), which is close to their
603 detection limits, as expected. This lower limit may have been influenced by the
604 ambient measurement conditions, where background nvPM concentrations were
605 non-negligible.

606 The agreement of the real-time measurements to within 30 % is larger than the
607 calibration uncertainties of the individual instruments, and suggests an influence
608 of systematic biases (e.g. in instrument calibration or penetration corrections).
609 There is no evidence of systematic differences between absorption and LII
610 measurements, which might have been hypothesized if coatings of volatile PM on
611 the light-absorbing nvPM had enhanced absorption. The larger scatter at lower
612 El_m values reflects the noise levels of the instruments. Both of these observations
613 are consistent with data reported previously for different engine types by Lobo et
614 al. (2016, 2020). The LII 300 and MSS+ from the North American Reference System
615 (NARS) have been widely used to characterize aircraft engine nvPM emissions. The
616 two CAPS instruments were independently calibrated and operated. The MSS+ and
617 PAX represent two photoacoustic spectrometers from different manufacturers,
618 operated by different teams, with different principles of calibration. The PAX was
619 also operated with a damaged capacitor on its printed circuit board. As noted in
620 Methods, these instruments operate on a variety of physical principles, including
621 photoacoustic spectroscopy (with two different designs), extinction-minus-
622 scattering, and laser-induced incandescence (cf. Section 3.3.3). Agreement
623 between these various principles also suggests that factors such as volatile
624 coatings on nvPM did not influence the instrument responses.

625 4.4.2 SMPS-based El_m

626 Figure 8b and Figure 9b are analogous to Figure 8a and Figure 9a, but for the
627 integrative nvPM measurements that do not fall into the real-time sampling

category. These data are plotted against the same geometric mean from Figure 8a. The dashed lines in Figure 9b represent the same ratios as in Figure 9a. Considering that the real-time instruments in Figure 8a were either calibrated to aerosol absorption or to aviation nvPM, we consider their accuracy as greater than the instruments in Figure 8b and consider departures from the 1:1 line as due to inaccuracy.

Most of the instruments in Figure 8b were accurate to within 30% of the reference, similar to Figure 8a, with the exception of the CS-SMPS and PSAP. This is summarized in Table 3, which shows the mean ratios of all data except engine idle (23% N1) with the geometric mean. Table 3 also includes the results of a linear regression against the geometric mean to facilitate comparison of our measurements with Kinsey et al. (2021), who performed linear regressions against simultaneous elemental carbon (EC) measurements (in our study, mass concentrations were too low to obtain EC measurements). The PSAP data are discussed in the next section. The CS-SMPS data were systematically higher than the geometric mean, potentially due to an overcorrection of the penetration of large particles to the SMPS.

Since the spread of nvPM EI_m reported by the two SMPS systems was smaller than the bias, their difference relative to the reference EI_m cannot be attributed to measurement biases (such as the limited size range detected by the instruments). Since the two SMPS systems showed different accuracies, their differences cannot be ascribed to a lack of constraints on the effective density of the nvPM particles (Momenimovahed and Olfert, 2015), which may vary with the monomer diameter (Abegglen et al., 2014; Durdina et al., 2014) and/or shape of soot aggregates. (We reiterate that our assumption of constant effective density is expected to introduce negligible uncertainty for the small soot particles emitted by aircraft turbine engines; Durdina et al., 2014). With respect to the real-time measurements, the TD-SMPS data are also consistent with previous measurements of aviation engine PSDs, which, however, were not corrected for diffusional particle loss (Lobo et al., 2015b, 2020). Careful measurement of the penetration functions used in these calculations would be required to confirm our interpretation.

4.4.3 Filter photometer-based EI_m from TAP and PSAP

Figure 8b and Figure 9b show that the TAP measurements were within the 30 % range observed for the real-time instruments, with a relative standard deviation (RSD) of 14 % (Table 3) for all data excluding the engine idle condition (23% N1). This provides high confidence for the use of the TAP for in-flight or field measurements of aircraft-engine nvPM mass emissions, when filter-loading corrections (Section 3.3.3) are correctly applied.

The PSAP, on the other hand, showed much greater variability, with an RSD of 36% (Table 3). This is substantially higher than the variability reported by a laboratory intercomparison of PSAP and CAPS PM_{SSA} (Perim De Faria et al., 2021) (that study did not report a statistic comparable to RSD). Although the PSAP has been observed to deviate up to a factor of two higher in cases of high organic aerosol loading or reduced filter transmission (Lack et al., 2013), our data are restricted to transmissions above 0.8. The fact that the PSAP shows great variability rather than a fixed offset indicates that the issue is not due to a systematic error such as an inaccurate MAC or flow rate calibration. We note that the TAP and PSAP were operated with reduced sample flow rates of 0.05 L min^{-1} and 0.1 L min^{-1} , respectively, (5 to 10% of nominal settings) to extend the life of their filter media while sampling the high soot concentrations in the aircraft exhaust. Under these conditions, detector noise and small fluctuations in sample flow have a magnified effect on resulting derived absorption coefficients. We suspect that the measurements would have been significantly more precise if the instruments had been operated at nominal flows, although this would have required changing filters after each test point. Consistent with our hypothesis, we note that Nakayama et al. (2010) observed substantially larger variability in PSAP measurements at 0.3 than at 0.7 standard litres per minute. We also note that Bond et al. (1999) did not observe an impact of flow rate when changing from 1 to 2 litres per minute.

Figure 10 plots as a function of particle GMD the same relative TAP and PSAP EI_m data shown in Figure 9b. No clear trend of this ratio with size is evident, although the measurements become somewhat more scattered at smaller sizes for the SAF1

data set, where signal to noise is lower (GMD and El_m were correlated, see the below discussion of Figure 12). Figure 10b includes the size-dependent PSAP correction function reported by Nakayama et al. (2010) (their Equation 8), with shading representing a 1σ uncertainty. Those authors predicted the true absorption values using Mie theory for nigrosin particles of diameter 100 to 600 nm and refractive index $1.685-0.285i$. Thus, their correction factor is conceptually equivalent to our $El_m/\text{mean-}El_m$. Extrapolating their correction function down from 100 nm to 15 nm gives values ranging from 4 to 8, whereas our measurements are close to 1.0. This discrepancy may be attributed primarily to the extrapolation, and possibly also to the fact that we have measured solid nvPM particles rather than liquid nigrosin. Overall, it is clear that the variability in our PSAP data is not sufficiently predicted by the GMD.

Overall, our data show that any possible size dependency in the TAP and PSAP response is smaller than the observed variability between samples. The TAP and PSAP data exhibit relative standard deviations (RSD) of 19% and 16%, respectively, for samples with GMD > 25 nm. Future studies may consider correcting PSAP and TAP measurements by the ratios shown in Table 3, which represent the ratio between the calibrated aerosol-phase nvPM mass measurements and the previously uncalibrated PSAP and TAP measurements, for data above $25 \text{ mg kg}_{\text{fuel}}^{-1}$ and $N1 > 40\%$.

4.5 Instrument performance for fuels with different composition

Figure 11 shows a category plot of the ratio $El_m/\text{mean-}El_m$ (that is, the ordinate of Figure 9) for the different instruments. Data below $100 \text{ mg / kg}_{\text{fuel}}$ have been excluded as this ratio reflects only noise in that region (Figure 9). The symbols have been sized by mean N1. The data have been coded by symbol and colour to reflect the 6 fuels used in this study, although JP-8 measurements are few in number due to the El_m of the data set (CFM56-2C1 with JP-8) being typically below $25 \text{ mg / kg}_{\text{fuel}}$.

Figure 11 shows that no substantial difference can be seen for these instruments for the nvPM El_m for fuels with different composition; the spread in the data for a

given fuel is larger than the difference between fuels. Outliers tend to be associated with low N1 (small symbols). Because low N1 corresponds to both lower concentrations (lower signal-to-noise) and lower exhaust velocities relative to ambient wind speeds, these outliers are not surprising.

The instruments in Figure 11 show a linear response to nvPM mass and operate on a range of physical principles. This observation indicates that no instrument was uniquely sensitive to changes in particle size over the observed range, since El_m was correlated with GMD (Figure 12), as is typical of aviation engines (Saffaripour et al., 2020). We note that the response of all of these instruments is proportional to the MAC of the sample, so that it remains possible that the sample MAC changed with GMD or El_m .

4.6 Influence of LII laser fluence

An additional experiment was performed to test the hypothesis that the laser fluence of the LII 300 may not be sufficiently high to heat nvPM to incandescence in aircraft-engine PM emissions from SAFs at different engine thrusts. The experimental design was similar to that of Yuan et al. (2022). This hypothesis is related to electron microscopy evidence (Vander Wal et al., 2014) showing that the degree of graphitization of aircraft-engine soot may be substantially lowered at low thrusts. A lower degree of graphitization may result in a lower LII signal if the 1064 nm MAC is lower (resulting in a lower maximum temperature being reached) or if part of the laser energy leads to carbon annealing rather than thermal excitation (Botero et al., 2021; Ugarte, 1992; Vander Wal and Choi, 1999). If correct, this hypothesis would mean that the nvPM concentrations reported by an LII 300 operated at reduced fluence would be lower than those of a reference LII 300. Higher fluences are also required for nvPM internally mixed with volatile PM, as some laser energy may be lost to volatile evaporation (Michelsen et al., 2015).

Figure 13a illustrates the experiment we performed to test this hypothesis. The figure presents data for SAF1 only; results for other fuels were similar. One "reduced-fluence" LII 300 was programmed to change its Q-switch delay from 140 μ s to 240 μ s, with a randomized order. In this experiment, lower Q-switch

delays corresponded to higher laser fluence; the lowest Q-switch delay was the optimal one for this system. Another “reference” LII 300 operated with no change to its Q-switch delay. Figure 13a shows that the reduced-fluence LII reported lower mass concentrations when its Q-switch delay was increased, but returned to the expected values when its Q-switch delay was reduced.

We defined R_{LII} as the ratio of nvPM mass concentrations reported by the reduced-fluence and reference LII 300 instruments. Figure 13b shows that R_{LII} was a function of Q-switch delay, and therefore laser fluence, for all engine thrust conditions. This observation is expected, since LII signals are lower at lower fluence (Michelsen et al., 2015) and since we calculated R_{LII} without taking this effect into account. We have verified in our laboratory that Q-switch delay is inversely proportional to laser fluence for this system and that saturation effects are negligible.

A trend of decreasing R_{LII} with decreasing N1 is evident at moderate and low Q-switch delays, which can be interpreted as indicating that the nvPM was more graphitic at higher N1 conditions. However, R_{LII} reached a plateau at high fluence (smaller Q-switch delay), which is the region where the LII 300 normally operates. This plateau was reached at all engine thrusts, with a broader range for the plateau at higher thrusts and a decreasing range as the thrust was lowered. Therefore, the LII 300 has sufficient fluence and can be expected to perform well for SAF blends at all engine thrust conditions.

5 Conclusions

For multiple instruments measuring nvPM number, size, and mass, we observed no evidence of anomalous instrument responses to the exhaust emissions produced by SAF blends relative to petroleum jet fuel (REFs) combustion in an IAE V2527-A5 engine. The GMD, GSD, and EI_{num} data for all fuels fell within 20%, 5%, and a factor of 2 of their mean, respectively. Anomalous instrumental responses would have resulted in two groups of data for these parameters, which was not observed. However, a difference between EI_{num} for instruments located on different-length sampling lines was noted and attributed to a greater sensitivity of EI_{num} than EI_m to the penetration function.

781

782 The majority of nvPM mass measurements by the real-time instruments (CAPS
783 PM_{SSA}, LII 300, MSS+, PAX) agreed to within 30% of their geometric mean
784 (reference mean), for EI_m above 100 mg/ kg_{fuel}. This lower limit corresponded to a
785 mass concentration of approximately 10 µg m⁻³ (the conversion of EI_m to mass
786 varies because the emitted [CO₂] varies), which was the noise level of these
787 instruments in our sampling setup. The ratio of each real-time measurement with
788 the reference mean was close to unity (maximally 1.24, minimally 0.78) and
789 indicated good precision (all RSDs ≤ 17%).

790

791 Integrative nvPM EI_m, calculated from PSD measurements or filter attenuation
792 (TAP and PSAP), fell within a factor of two of the reference mean. The ratio of each
793 integrative measurement with the reference mean was further from unity
794 (maximally 1.50, minimally 0.88) and variability was higher precision (all RSDs
795 ≤ 36%). The variability in TAP data was notably low at 14%, and the variability in
796 PSAP data was notably high at 36%, likely due to its operation at a reduced flow
797 rate.

798

799 Two other instrument- and fuel composition-specific observations were made. A
800 dedicated experiment showed that changing the laser fluence of an LII 300 could
801 influence its reported nvPM mass concentrations at low to moderate fluences. By
802 maintaining sufficiently high fluence a plateau region was established, irrespective
803 of thrust or fuel, where reported nvPM mass concentrations were stable and not
804 influenced by experimental conditions. Second, additional measurements of
805 emissions from JP-8 fuel combusted in a CFM56-2C1 engine indicated the presence
806 of very high concentrations of volatile nucleation-mode particles with
807 diameter < 20 nm. These measurements reflect a different engine, as well as a fuel
808 with a factor 20 higher sulfur content, and the increased total PM number
809 concentration is most likely attributable to the sulfur.

810

811 Overall, this study found that real-time instruments for the measurement of nvPM
812 emissions in aviation turbine engines are comparable whether conventional fuels
813 or SAFs are used. Since all real-time measurements were influenced by the MAC

814 and no independent measurement of nvPM mass was made, no conclusions about
815 the variability thereof can be made from this study.

816 5.1 Author contributions

817 BEA, PLC, TS, PL, GJS, PDW, and RML designed the study. JCC, TS, PLC, GJS, ECC, SA,
818 PDW, RML, ZY, AF, MT, DS, WL, CR, PO, MS, and PL took the measurements. JCC, TS,
819 BEA, RHM, MAS, ECC, SA, ZY analyzed the data with input from GJS, PL, RML, and
820 AF. JCC prepared the figures. JCC and PL drafted the manuscript. All authors
821 discussed the data interpretation and presentation.

822 5.2 Competing interests

823 RML and AF are employed by ARI, which produces the CAPS PM_{SSA} commercially.
824 ZY was employed by ARI at the time of the study.

825 5.3 Acknowledgements

826 We acknowledge the efforts of the flight and ground crews of the DLR ATRA, the
827 NASA DC8, and the U.S. Air Force 86th Air Wing. We thank the ground staff of
828 Ramstein Air Base for their operational support during this experiment.

829 5.4 Financial support

830 This research received funding from the Transport Canada project “TC Aviation —
831 nvPM from renewable and conventional fuels”. The campaign was funded by the
832 DLR aeronautics program in the framework of the project “Emission and Climate
833 Impact of Alternative Fuels (ECLIF)”. MS&T and ARI received support from the U.S.
834 Federal Aviation Administration (FAA) through the Aviation Sustainability Center
835 (ASCENT) – a U.S. FAA-NASA- U.S. DoD-Transport Canada- U.S. EPA sponsored
836 Center of Excellence for Alternative Jet Fuels and Environment under Grant No. 13-
837 C-AJFE-MST, Amendment 010. A.F. was supported by funds from ARI. ATRA
838 operational and fuel costs along with DLR scientists’ participation was funded by
839 the DLR aeronautics program in the framework of the project “Emission and
840 Climate Impact of Alternative Fuels (ECLIF)”. The U.S. FAA Office of Environment
841 and Energy and the National Aeronautics and Space Administration Aeronautics
842 Research Mission Directorate supported field and DC-8 operations, and
843 participation of the U.S. researchers in the project.

5.5 Data availability

The data presented in Figures 4 to 10 are available in the Zenodo repository at <https://sandbox.zenodo.org/record/950512> as a spreadsheet file. Other data are available from the authors upon request.

6 References

- ASTM D4054: Practice for Evaluation of New Aviation Turbine Fuels and Fuel Additives. Conshohocken, PA: ASTM International; 2019. doi: 10.1520/D4054-19.
- ASTM D7566: Specification for Aviation Turbine Fuel Containing Synthesized Hydrocarbons. Conshohocken, PA: ASTM International; 2020. doi: 10.1520/D7566-20
- International Civil Aviation Organization (2017). International Standards and Recommended Practices – Annex 16 to the Convention on International Civil Aviation: Environmental Protection, Volume II - Aircraft Engine Emissions, 4th ed., Montreal, QC, Canada.
- Abegglen, M., Durdina, L., Mensah, A., Brem, B., Corbin, J., Wang, J., Lohmann, U. and Sierau, B.: Effective density measurements of fresh particulate matter emitted by an aircraft engine, in EGU General Assembly Conference Abstracts, vol. 16, p. 14367., 2014.
- ASTM D4054: Practice for Evaluation of New Aviation Turbine Fuels and Fuel Additives. Conshohocken, PA: ASTM International; 2019. doi: 10.1520/D4054-19.
- ASTM D7566: Specification for Aviation Turbine Fuel Containing Synthesized Hydrocarbons. Conshohocken, PA: ASTM International; 2020. doi: 10.1520/D7566-20
- Beyersdorf, A. J., Timko, M. T., Ziemba, L. D., Bulzan, D., Corporan, E., Herndon, S. C., Howard, R., Miake-Lye, R., Thornhill, K. L., Winstead, E., Wey, C., Yu, Z. and Anderson, B. E.: Reductions in aircraft particulate emissions due to the use of Fischer-Tropsch fuels, *Atmos. Chem. Phys.*, 14(1), 11–23, doi:10.5194/acp-14-11-2014.
- Bond, T. C. and Bergstrom, R. W.: Light absorption by carbonaceous particles: An investigative review, *Aerosol Sci. Technol.*, 40(1), 27–67, doi:10.1080/02786820500421521, 2006.
- Bond, T. C., Anderson, T. L. and Campbell, D.: Calibration and Intercomparison of Filter-Based Measurements of Visible Light Absorption by Aerosols, *Aerosol Sci. Technol.*, 30(6), 582–600, doi:10.1080/027868299304435, 1999.
- Botero, M. L., Akroyd, J., Chen, D., Kraft, M. and Agudelo, J. R.: On the thermophoretic sampling and TEM-based characterisation of soot particles in flames, *Carbon N. Y.*, 171, 711–722, doi:10.1016/j.carbon.2020.09.074, 2021.
- Brem, B. T., Durdina, L., Siegerist, F., Beyerle, P., Bruderer, K., Rindlisbacher, T., Rocci-Denis, S., Andac, M. G., Zelina, J., Penanhoat, O. and Wang, J.: Effects of Fuel Aromatic Content on Nonvolatile Particulate Emissions of an In-Production Aircraft Gas Turbine, *Environ. Sci. Technol.*, 49(22), 13149–13157, doi:10.1021/acs.est.5b04167, 2015.
- Cain, J., Dewitt, M. J., Blunck, D., Corporan, E., Striebich, R., Anneken, D., Klingshirn, C., Roquemore, W. M. and Vander Wal, R.: Characterization of gaseous and particulate emissions from a turboshaft engine burning conventional, alternative, and surrogate fuels, *Energy Fuels*, 27(4), 2290–2302, doi:10.1021/ef400009c, 2013.
- Catalytic Stripper CS015 Instrument Manual, Catalytic Instruments GmbH, 2014.

Clarke, A. D.: A thermo-optic technique for in situ analysis of size-resolved aerosol physicochemistry, *Atmos. Environ. Part A, Gen. Top.*, 25(3–4), 635–644, doi:10.1016/0960-1686(91)90061-B, 1991.

Corporan, E., Edwards, T., Shafer, L., Dewitt, M. J., Klingshirn, C., Zabarnick, S., West, Z., Striebich, R., Graham, J. and Klein, J.: Chemical, thermal stability, seal swell, and emissions studies of alternative jet fuels, *Energy Fuels*, 25(3), 955–966, doi:10.1021/ef101520v, 2011.

Durand, E., Lobo, P., Crayford, A., Sevcenco, Y. and Christie, S.: Impact of fuel hydrogen content on non-volatile particulate matter emitted from an aircraft auxiliary power unit measured with standardised reference systems, *Fuel*, 287, 119637, doi:10.1016/j.fuel.2020.119637, 2021.

Durdina, L., Brem, B. T., Abegglen, M., Lobo, P., Rindlisbacher, T., Thomson, K. A., Smallwood, G. J., Hagen, D. E., Sierau, B. and Wang, J.: Determination of PM mass emissions from an aircraft turbine engine using particle effective density, *Atmos. Environ.*, 99, 500–507, doi:10.1016/j.atmosenv.2014.10.018, 2014.

Elser, M., Brem, B. T., Durdina, L., Schönenberger, D., Siegerist, F., Fischer, A. and Wang, J.: Chemical composition and radiative properties of nascent particulate matter emitted by an aircraft turbofan burning conventional and alternative fuels, *Atmos. Chem. Phys.*, 19(10), 6809–6820, doi:10.5194/acp-19-6809-2019, 2019.

Gagné, S., Couillard, M., Gajdosechova, Z., Momenimovahed, A., Smallwood, G., Mester, Z., Thomson, K., Lobo, P. and Corbin, J. C.: Ash-Decorated and Ash-Painted Soot from Residual and Distillate-Fuel Combustion in Four Marine Engines and One Aviation Engine, *Environ. Sci. Technol.*, 55, 6584–6593, doi:10.1021/acs.est.0c07130, 2021.

Hileman, J. I. and Stratton, R. W.: Alternative jet fuel feasibility, *Transp. Policy*, 34, 52–62, doi:10.1016/j.tranpol.2014.02.018, 2014.

Hinds, W. C.: *Aerosol technology: properties, behavior, and measurement of airborne particles*, John Wiley & Sons., 1999.

Huang, C. H. and Vander Wal, R. L.: Effect of soot structure evolution from commercial jet engine burning petroleum based JP-8 and synthetic HRJ and FT fuels, *Energy Fuels*, 27(8), 4946–4958, doi:10.1021/ef400576c, 2013.

ICAO: *International Standards and Recommended Practices – Annex 16 to the Convention on International Civil Aviation: Environmental Protection, Volume II - Aircraft Engine Emissions*, Montreal, QC., 2017.

International Civil Aviation Organization (2017). *International Standards and Recommended Practices – Annex 16 to the Convention on International Civil Aviation: Environmental Protection, Volume II - Aircraft Engine Emissions*, 4th ed., Montreal, QC, Canada.

Kiliç, D., El Haddad, I., Brem, B. T., Bruns, E., Bozetti, C., Corbin, J., Durdina, L., Huang, R. J., Jiang, J., Klein, F., Lavi, A., Pieber, S. M., Rindlisbacher, T., Rudich, Y., Slowik, J. G., Wang, J., Baltensperger, U. and Prévôt, A. S. H.: Identification of secondary aerosol precursors emitted by an aircraft turbofan, *Atmos. Chem. Phys.*, 18(10), 7379–7391, doi:10.5194/acp-18-7379-2018, 2018.

Kinsey, J. S., Timko, M. T., Herndon, S. C., Wood, E. C., Yu, Z., Miake-Lye, R. C., Lobo, P., Whitefield, P., Hagen, D., Wey, C., Anderson, B. E., Beyersdorf, A. J., Hudgins, C. H., Thornhill, K. L., Edward, W., Howard, R., Bulzan, D. I., Tacina, K. B. and Knighton, W. B.: Determination of the emissions from an aircraft auxiliary power unit (APU) during the alternative aviation fuel experiment (AAFEX), *J. Air Waste Manag. Assoc.*, 62(4), 420–430, doi:10.1080/10473289.2012.655884, 2012.

934 Kinsey, J. S., Giannelli, R., Howard, R., Hoffman, B., Frazee, R., Aldridge, M., Leggett, C.,
 935 Stevens, K., Kittelson, D., Silvis, W., Stevens, J., Lobo, P., Achterberg, S., Swanson, J.,
 936 Thomson, K., McArthur, T., Hagen, D., Trueblood, M., Wolff, L., Liscinsky, D., Arey, R.,
 937 Cerully, K., Miake-Lye, R., Onasch, T., Freedman, A., Bachalo, W., Payne, G. and Durllicki, M.:
 938 Assessment of a regulatory measurement system for the determination of the non-volatile
 939 particulate matter emissions from commercial aircraft engines, *J. Aerosol Sci.*, 154,
 940 105734, doi:10.1016/j.jaerosci.2020.105734, 2021.

941 Kumal, R. R., Liu, J., Gharpure, A., Vander Wal, R. L., Kinsey, J. S., Giannelli, B., Stevens, J.,
 942 Leggett, C., Howard, R., Forde, M., Zelenyuk, A., Suski, K., Payne, G., Manin, J., Bachalo, W.,
 943 Frazee, R., Onasch, T. B., Freedman, A., Kittelson, D. B. and Swanson, J. J.: Impact of Biofuel
 944 Blends on Black Carbon Emissions from a Gas Turbine Engine, *Energy Fuels*, 34(4), 4958–
 945 4966, doi:10.1021/acs.energyfuels.0c00094, 2020.

946 Lack, D. A., Moosmüller, H., McMeeking, G. R., Chakrabarty, R. K. and Baumgardner, D.:
 947 Characterizing elemental, equivalent black, and refractory black carbon aerosol particles:
 948 a review of techniques, their limitations and uncertainties, *Anal. Bioanal.Chem.*, 406(1),
 949 99–122, doi:10.1007/s00216-013-7402-3, 2014.

950 Liati, A., Schreiber, D., Alpert, P. A., Liao, Y., Brem, B. T., Corral Arroyo, P., Hu, J., Jonsdottir,
 951 H. R., Ammann, M. and Dimopoulos Eggenschwiler, P.: Aircraft soot from conventional
 952 fuels and biofuels during ground idle and climb-out conditions: Electron microscopy and
 953 X-ray micro-spectroscopy, *Environ. Pollut.*, 247, 658–667,
 954 doi:10.1016/j.envpol.2019.01.078, 2019.

955 Liu, F., Yon, J., Fuentes, A., Lobo, P., Smallwood, G. J. and Corbin, J. C.: Review of recent
 956 literature on the light absorption properties of black carbon: Refractive index, mass
 957 absorption cross section, and absorption function, *Aerosol Sci. Technol.*, 54(1), 33–51,
 958 doi:10.1080/02786826.2019.1676878, 2020.

959 Lobo, P., Hagen, D. E. and Whitefield, P. D.: Comparison of PM emissions from a commercial
 960 jet engine burning conventional, biomass, and fischer-tropsch fuels, *Environ. Sci. Technol.*,
 961 45(24), doi:10.1021/es201902e, 2011.

962 Lobo, P., Christie, S., Khandelwal, B., Blakey, S. G. and Raper, D. W.: Evaluation of Non-
 963 volatile Particulate Matter Emission Characteristics of an Aircraft Auxiliary Power Unit
 964 with Varying Alternative Jet Fuel Blend Ratios, *Energy Fuels*, 29(11), 7705–7711,
 965 doi:10.1021/acs.energyfuels.5b01758, 2015a.

966 Lobo, P., Durdina, L., Smallwood, G. J., Rindlisbacher, T., Siegerist, F., Black, E. A., Yu, Z.,
 967 Mensah, A. A., Hagen, D. E., Miake-Lye, R. C., Thomson, K. A., Brem, B. T., Corbin, J. C.,
 968 Abegglen, M., Sierau, B., Whitefield, P. D. and Wang, J.: Measurement of aircraft engine non-
 969 volatile PM emissions: Results of the Aviation-Particle Regulatory Instrumentation
 970 Demonstration Experiment (A-PRIDE) 4 campaign, *Aerosol Sci. Technol.*, 49(7), 472–484,
 971 doi:10.1080/02786826.2015.1047012, 2015b.

972 Lobo, P., Hagen, D. E., Whitefield, P. D. and Raper, D.: PM emissions measurements of in-
 973 service commercial aircraft engines during the Delta-Atlanta Hartsfield Study, *Atmos.*
 974 *Environ.*, 104, 237–245, doi:10.1016/j.atmosenv.2015.01.020, 2015c.

975 Lobo, P., Condevaux, J., Yu, Z., Kuhlmann, J., Hagen, D. E., Miake-Lye, R. C., Whitefield, P. D.
 976 and Raper, D. W.: Demonstration of a Regulatory Method for Aircraft Engine Nonvolatile
 977 PM Emissions Measurements with Conventional and Isoparaffinic Kerosene fuels, *Energy*
 978 *Fuels*, 30(9), 7770–7777, doi:10.1021/acs.energyfuels.6b01581, 2016.

979 Lobo, P., Durdina, L., Brem, B. T., Crayford, A. P., Johnson, M. P., Smallwood, G. J., Siegerist,
 980 F., Williams, P. I., Black, E. A., Llamedo, A., Thomson, K. A., Trueblood, M. B., Yu, Z., Hagen, D.
 981 E., Whitefield, P. D., Miake-Lye, R. C. and Rindlisbacher, T.: Comparison of standardized
 982 sampling and measurement reference systems for aircraft engine non-volatile particulate

983 matter emissions, *J. Aerosol Sci.*, 145, 105557, doi:10.1016/j.jaerosci.2020.105557, 2020.

984 Masiol, M. and Harrison, R. M.: Aircraft engine exhaust emissions and other airport-related
 985 contributions to ambient air pollution: A review, *Atmos. Environ.*, 95, 409–455,
 986 doi:10.1016/j.atmosenv.2014.05.070, 2014.

987 Michelsen, H. A., Schulz, C., Smallwood, G. J. and Will, S.: Laser-induced incandescence:
 988 Particulate diagnostics for combustion, atmospheric, and industrial applications, *Prog.*
 989 *Energy Combust. Sci.*, 51, 2–48, doi:10.1016/j.pecs.2015.07.001, 2015.

990 Modini, R. L., Corbin, J. C., Brem, B. T., Irwin, M., Bertò, M., Pileci, R. E., Fetfatzis, P.,
 991 Eleftheriadis, K., Henzing, B., Moerman, M. M., Liu, F., Müller, T. and Gysel-Beer, M.:
 992 Detailed characterization of the CAPS single-scattering albedo monitor (CAPS PMssa) as a
 993 field-deployable instrument for measuring aerosol light absorption with the extinction-
 994 minus-scattering method, *Atmos. Meas. Tech.*, 14(2), doi:10.5194/amt-14-819-2021,
 995 2021.

996 Momenimovahed, A. and Olfert, J. S.: Effective Density and Volatility of Particles Emitted
 997 from Gasoline Direct Injection Vehicles and Implications for Particle Mass Measurement,
 998 *Aerosol Sci. Technol.*, 49(11), 1051–1062, doi:10.1080/02786826.2015.1094181, 2015.

999 Moore, R. H., Thornhill, K. L., Weinzierl, B., Sauer, D., D’Ascoli, E., Kim, J., Lichtenstern, M.,
 1000 Scheibe, M., Beaton, B., Beyersdorf, A. J., Barrick, J., Bulzan, D., Corr, C. A., Crosbie, E., Jurkat,
 1001 T., Martin, R., Riddick, D., Shook, M., Slover, G., Voigt, C., White, R., Winstead, E., Yasky, R.,
 1002 Ziemba, L. D., Brown, A., Schlager, H. and Anderson, B. E.: Biofuel blending reduces particle
 1003 emissions from aircraft engines at cruise conditions, *Nature*, 543(7645), 411–415,
 1004 doi:10.1038/nature21420, 2017.

1005 Nakayama, T., Kondo, Y., Moteki, N., Sahu, L. K., Kinase, T., Kita, K. and Matsumi, Y.: Size-
 1006 dependent correction factors for absorption measurements using filter-based
 1007 photometers: PSAP and COSMOS, *J. Aerosol Sci.*, 41(4), 333–343,
 1008 doi:10.1016/j.jaerosci.2010.01.004, 2010.

1009 Nakayama, T., Suzuki, H., Kagamitani, S., Ikeda, Y., Uchiyama, A. and Matsumi, Y.:
 1010 Characterization of a Three Wavelength Photoacoustic Soot Spectrometer ({PASS}-3) and
 1011 a Photoacoustic Extinctionmeter ({PAX}), *J. Meteorol. Soc. Japan. Ser. {II}*, 93(2), 285–308,
 1012 doi:10.2151/jmsj.2015-016, 2015.

1013 Ogren, J. A., Wendell, J., Andrews, E. and Sheridan, P. J.: Continuous light absorption
 1014 photometer for long-Term studies, *Atmos. Meas. Tech.*, 10(12), 4805–4818,
 1015 doi:10.5194/amt-10-4805-2017, 2017.

1016 Onasch, T. B., Massoli, P., Keabian, P. L., Hills, F. B., Bacon, F. W. and Freedman, A.: Single
 1017 Scattering Albedo Monitor for Airborne Particulates, *Aerosol Sci. Technol.*, 49(4), 267–279,
 1018 doi:10.1080/02786826.2015.1022248, 2015.

1019 Perim De Faria, J., Bundke, U., Freedman, A., Onasch, T. B. and Petzold, A.: Laboratory
 1020 validation of a compact single-scattering albedo (SSA) monitor, *Atmos. Meas. Tech.*, 14(2),
 1021 1635–1653, doi:10.5194/amt-14-1635-2021, 2021.

1022 Petzold, A., Ogren, J. A., Fiebig, M., Laj, P., Li, S.-M., Baltensperger, U., Holzer-Popp, T., Kinne,
 1023 S., Pappalardo, G., Sugimoto, N., Wehrli, C., Wiedensohler, A. and Zhang, X.-Y.:
 1024 Recommendations for the interpretation of “black carbon” measurements, *Atmos. Chem.*
 1025 *Phys.*, 13(16), 8365–8379, doi:10.5194/acp-13-8365-2013, 2013.

1026 SAE International. Aerospace Information Report (AIR) 6241 . Procedure for the
 1027 Continuous Sampling and Measurement of Non-Volatile Particle Emissions from Aircraft
 1028 Turbine Engines. Warrendale, PA, 2013. <https://doi.org/10.4271/AIR6241>

1029 SAE international. Aerospace Recommended Practice (ARP) 6320 - Procedure for the
 1030 Continuous Sampling and Measurement of Non-Volatile Particulate Matter Emissions from
 1031 Aircraft Turbine Engines, Warrendale, PA, 2018. <https://doi.org/10.4271/ARP6320>.

1032 SAE International. Aerospace Information Report (AIR) 6504 - Procedure for the
 1033 Calculation of Sampling System Penetration Functions and System Loss Correction
 1034 Factors, Warrendale, PA, 2017. <https://doi.org/10.4271/AIR6504>

1035 SAE International. Aerospace Recommended Practice (ARP) 6481- Procedure for the
 1036 Calculation of Sampling Line Penetration Functions and Line Loss Correction Factors,
 1037 Warrendale, PA, 2019. <https://doi.org/10.4271/ARP6481>

1038 Saffaripour, M., Thomson, K. A., Smallwood, G. J. and Lobo, P.: A review on the
 1039 morphological properties of non-volatile particulate matter emissions from aircraft
 1040 turbine engines, *J. Aerosol Sci.*, 139, doi:10.1016/j.jaerosci.2019.105467, 2020.

1041 Schindler, W., Haisch, C., Beck, H. A., Niessner, R., Jacob, E. and Rothe, D.: A photoacoustic
 1042 sensor system for time resolved quantification of diesel soot emissions, *SAE Technical*
 1043 *Paper* 2004-01-0968, SAE International., doi:10.4271/2004-01-0968, 2004.

1044 Schripp, T., Anderson, B. E., Bauder, U., Rauch, B., Corbin, J. C., Smallwood, G. J., Lobo, P.,
 1045 Crosbie, E., Shook, M. E., Miake-Lye, R., Yu, Z., Freedman, A., Whitefield, P. D., Robinson, C.
 1046 E., Achterberg, S. L., Köhler, M., Oßwald, P., Grein, T., Sauer, D., Voigt, C., Schlager, H.,
 1047 LeClercq, P. Aircraft engine particulate matter and gaseous emissions from sustainable
 1048 aviation fuels: results from ground-based measurements during the NASA/DLR Campaign
 1049 ECLIF2/ND-MAX. Submitted to *Fuel*. 2022.

1050 Schripp, T., Anderson, B., Crosbie, E. C., Moore, R. H., Herrmann, F., Oßwald, P., Wahl, C.,
 1051 Kapernaum, M., Köhler, M., Le Clercq, P., Rauch, B., Eichler, P., Mikoviny, T. and Wisthaler,
 1052 A.: Impact of Alternative Jet Fuels on Engine Exhaust Composition during the 2015 ECLIF
 1053 Ground-Based Measurements Campaign, *Environ. Sci. Technol.*, 52(8), 4969–4978,
 1054 doi:10.1021/acs.est.7b06244, 2018.

1055 Schripp, T., Herrmann, F., Oßwald, P., Köhler, M., Zschocke, A., Weigelt, D., Mroch, M. and
 1056 Werner-Spatz, C.: Particle emissions of two unblended alternative jet fuels in a full scale jet
 1057 engine, *Fuel*, 256, 115903, doi:10.1016/j.fuel.2019.115903, 2019.

1058 Snelling, D. R., Smallwood, G. J., Liu, F., Gülder, Ö. L. and Bachalo, W. D.: A calibration-
 1059 independent laser-induced incandescence technique for soot measurement by detecting
 1060 absolute light intensity, *Appl. Opt.*, 44(31), 6773, doi:10.1364/ao.44.006773, 2005.

1061 Timko, M. T., Yu, Z., Onasch, T. B., Wong, H. W., Miake-Lye, R. C., Beyersdorf, A. J., Anderson,
 1062 B. E., Thornhill, K. L., Winstead, E. L., Corporan, E., Dewitt, M. J., Klingshirn, C. D., Wey, C.,
 1063 Tacina, K., Liscinsky, D. S., Howard, R. and Bhargava, A.: Particulate emissions of gas
 1064 turbine engine combustion of a fischer-tropsch synthetic fuel, *Energy Fuels*, 24(11), 5883–
 1065 5896, doi:10.1021/ef100727t, 2010.

1066 Timko, M. T., Fortner, E., Franklin, J., Yu, Z., Wong, H. W., Onasch, T. B., Miake-Lye, R. C. and
 1067 Herndon, S. C.: Atmospheric measurements of the physical evolution of aircraft exhaust
 1068 plumes, *Environ. Sci. Technol.*, 47(7), 3513–3520, doi:10.1021/es304349c, 2013.

1069 Trueblood, M. B., Lobo, P., Hagen, D. E., Achterberg, S. C., Liu, W. and Whitefield, P. D.:
 1070 Application of a hygroscopicity tandem differential mobility analyzer for characterizing
 1071 PM emissions in exhaust plumes from an aircraft engine burning conventional and
 1072 alternative fuels, *Atmos. Chem. Phys.*, 18(23), doi:10.5194/acp-18-17029-2018, 2018.

1073 Ugarte, D.: Curling and closure of graphitic networks under electron-beam irradiation,
 1074 *Nature*, 359(6397), 707–709, doi:10.1038/359707a0, 1992.

1075 Virkkula, A.: Erratum: Calibration of the 3-wavelength particle soot absorption

1076 photometer (3λ PSAP) (Aerosol Science and Technology (2002) 39 (68-83)), Aerosol Sci.
 1077 Technol., 44(8), 706–712, doi:10.1080/02786826.2010.482110, 2010.

1078 Vozka, P., Vrtiška, D., Šimáček, P. and Kilaz, G.: Impact of Alternative Fuel Blending
 1079 Components on Fuel Composition and Properties in Blends with Jet A, Energy Fuels, 33(4),
 1080 3275–3289, doi:10.1021/acs.energyfuels.9b00105, 2019.

1081 Vander Wal, R. L. and Choi, M. Y.: Pulsed laser heating of soot: morphological changes,
 1082 Carbon N. Y., 37(2), 231–239, doi:10.1016/S0008-6223(98)00169-9, 1999.

1083 Vander Wal, R. L., Bryg, V. M. and Huang, C.-H.: Aircraft engine particulate matter: Macro-
 1084 micro- and nanostructure by HRTEM and chemistry by XPS, Combust. Flame, 161(2), 602–
 1085 611, doi:10.1016/j.combustflame.2013.09.003, 2014.

1086 Williams, P. I., Allan, J. D., Lobo, P., Coe, H., Christie, S., Wilson, C., Hagen, D., Whitefield, P.,
 1087 Raper, D. and Rye, L.: Impact of alternative fuels on emissions characteristics of a gas
 1088 turbine engine - Part 2: Volatile and semivolatile particulate matter emissions, Environ.
 1089 Sci. Technol., 46(19), doi:10.1021/es301899s, 2012.

1090 Wilson, G. R., Edwards, T., Corporan, E. and Freerks, R. L.: Certification of alternative
 1091 aviation fuels and blend components, Energy Fuels, 27(2), 962–966,
 1092 doi:10.1021/ef301888b, 2013.

1093 Yuan, R., Lobo, P., Smallwood, G. J., Johnson, M. P., Parker, M. C., Butcher, D., &
 1094 Spencer, A. (2022). Measurement of black carbon emissions from multiple engine
 1095 and source types using laser-induced incandescence: sensitivity to laser fluence.
 1096 Atmospheric Measurement Techniques, 15(2), 241–259. [doi:10.5194/amt-15-241-](https://doi.org/10.5194/amt-15-241-2022)
 1097 [2022](https://doi.org/10.5194/amt-15-241-2022). 2022.

1098

1099 7 Figures and Tables

1100 Table 1. Properties of the fuels used for the ground-based measurements (fuel
1101 samples acquired from wing-tank after test).

Property	Method	JP-8	REF3	REF4	SAF1	SAF2	SAF3
Aromatics	ASTM	19.9	18.6	16.5	8.5	9.5	15.2
[vol%]	D1319						
Hydrogen H	ASTM	13.86	13.65	14.08	14.40	14.51	14.04
[mass%]	D7171						
Sulphur, total	ISO	1240	105	5.7	56.8	4.1	58.6
[ppm]	20884						
Naphthalenes	ASTM	1.49	1.17	0.13	0.61	0.05	0.64
[mass%]	D1840						
Smoke point	ASTM	23.0	23.0	27.0	30.0	30.0	28.0
[mm]	D1322						

1102

1103
1104

Table 2. Instruments used to measure nvPM and key measured properties. All instruments reported data at 1 second intervals except the SMPs (45 second intervals for NRC and DLR, 60 seconds for NASA) and filter samplers. Instrument abbreviations are defined in the text.

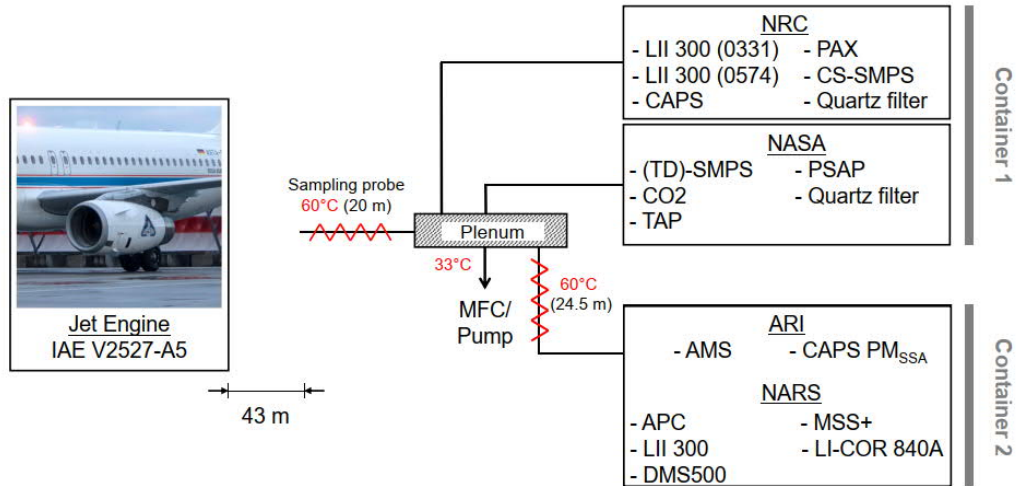
Operator	Instrument	Acronym	Species measured	Sampling duration [s]	Units	Penetration functions ^d
NASA	Particle soot absorption photometer	PSAP	nvPM ^a mass	1	µg m ⁻³	1
	Tricolor absorption photometer	TAP	nvPM ^a mass	1	µg m ⁻³	1
	Scanning mobility particle sizer	SMPS	Total PSD (10 to 278 nm)	45	particles cm ⁻³ , and µg m ⁻³	1
	Thermo-denuder with SMPS	TD-SMPS	nvPM PSD ^b (10 to 278 nm)	45	µg m ⁻³	1, 4
	CO ₂ sensor	LI-COR 7000	CO ₂	1	ppmv	-
NRC	Cavity-attenuated phase shift PM _{SSA} monitor (660 nm)	CAPS (NRC)	nvPM ^a mass	1	µg m ⁻³	1
	Photoacoustic extinctions	PAX	nvPM ^a mass	1	µg m ⁻³	1
	Laser-induced-incandescence	LII 300 (NRC; 2x)	nvPM ^b mass	1	µg m ⁻³	1
	Catalytic stripper SMPS	CS-SMPS	nvPM PSD (8.6 to 278 nm)	45	particles cm ⁻³	1, 3
MST (NARS)	AVL Particle Counter Advanced	APC	nvPM number	1	particles cm ⁻³	1, 2
	Micro Soot Sensor	MSS Plus	nvPM ^a mass	1	µg m ⁻³	1, 2
	Laser-induced-incandescence	LII-300 (NARS)	nvPM ^c mass	1	µg m ⁻³	1, 2
	CO ₂ sensor	LI-COR 840A	CO ₂	1	ppm	-
	Differential mobility spectrometer	DMS500	Total PSD (5 to 1000 nm)	1	particles cm ⁻³	1, 2
ARI	Cavity-attenuated phase shift PM _{SSA} monitor (630 nm)	CAPS (ARI)	nvPM ^a mass	1	µg m ⁻³	1, 2

1105
1106

^anvPM measured via particulate absorption as equivalent BC (eBC). ^bParticle size distribution, here measured with respect to mobility diameter. ^cnvPM measured via laser-induced incandescence as refractory BC (rBC). ^dNumbers are indices corresponding to the penetration functions shown in Figure 4.

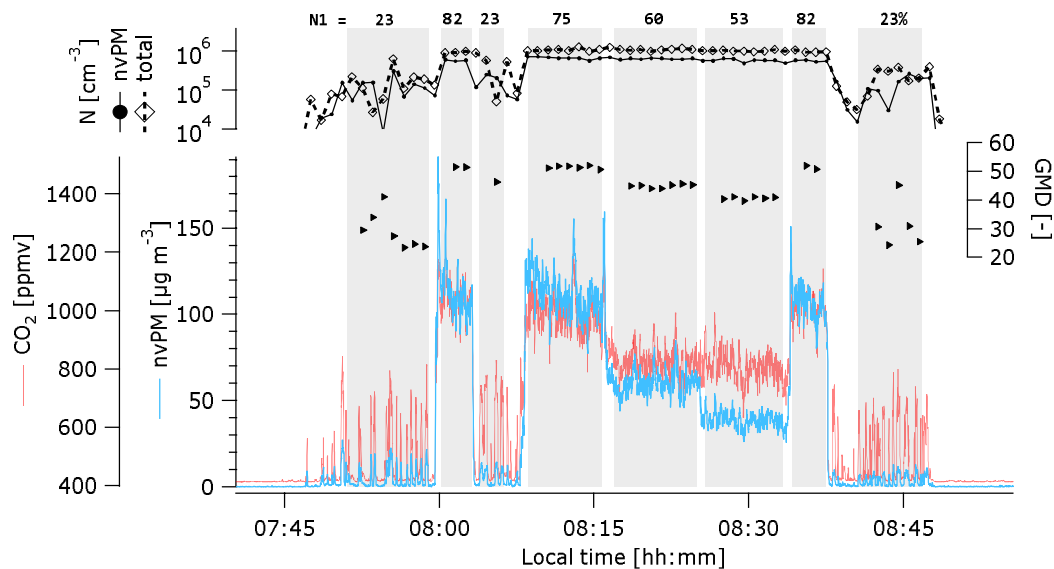
Table 3. Summary of the ratios between the EI_m of individual instruments and the geometric mean of the Group 1 (real time) instruments. The corresponding raw data are shown in Figure 11. Regression: linear regression against Group 1 geometric mean weighted by standard deviations, with $k = 2$ uncertainties from fit. SD: standard deviation. RSD: Relative SD. Group 1: real time instruments. Group 2: integrative instruments.

Group	Instrument	EI_{mass} Ratio vs. Group 1			Regression vs. Group 1	
		Mean	SD	RSD [%]	Intercept	Slope
1	CAPS PM_{SSA} (ARI)	0.84	0.08	10	12 ± 19	0.8 ± 0.1
1	CAPS PM_{SSA} (NRC)	0.99	0.09	9	-0.3 ± 0.8	1.01 ± 0.04
1	LII (NARS)	1.24	0.18	15	27 ± 6	1.03 ± 0.04
1	LII (NRC-0331)	1.07	0.1	9	-15 ± 42	1.17 ± 0.16
1	LII (NRC-0574)	0.78	0.08	10	-17.1 ± 2	0.88 ± 0.08
1	MSS+	1.07	0.14	13	17.8 ± 5	0.92 ± 0.04
1	PAX	1.06	0.18	17	-15 ± 1	1.21 ± 0.02
2	CS-SMPS	1.50	0.27	18	12 ± 22	1.02 ± 0.12
2	TD-SMPS	1.14	0.26	23	-5 ± 1	1.47 ± 0.04
2	PSAP	0.89	0.32	36	8 ± 16	0.82 ± 0.08
2	TAP	0.88	0.12	14	6 ± 6	0.75 ± 0.02



1115

1116 Figure 1. Schematic of sampling configuration behind the DLR ATRA aircraft. The length
1117 and flow rate of sampling lines from the manifold to the various instruments varied as
1118 described in the text. The NRC and NASA instruments were all placed within Container 1,
1119 while the NARS and ARI instruments were placed in Container 2. For simplicity, the figure
1120 omits a short heated line connecting the first plenum to the NARS. The ARI instruments
1121 were downstream of all NARS instruments except the DMS500 (see Lobo et al., 2016 for
1122 detailed NARS diagram). NARS = North American Reference System.



1123

1124 Figure 2. Illustration of a typical test run. Variation in the CO_2 concentration was not due
1125 to instrument noise, as illustrated by the CO_2 measurements prior to and following
1126 sampling. A representative nvPM mass instrument is shown by the blue trace. Sizing
1127 information (GMD) is shown by the black symbols (triangles: GMD; diamonds with dashed
1128 line: total PM number; spheres with solid line: nvPM number measured with the CS-
1129 SMPS).

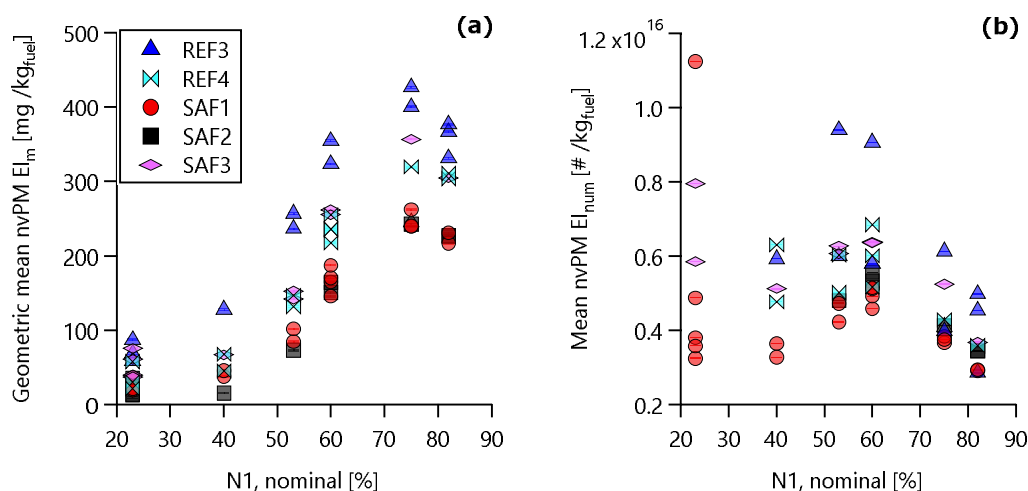


Figure 3. Relationship between nvPM (a) EI_m and (b) EI_{num} with N1 for all data obtained with the V2527-A5 engine. The trends shown in this plot are discussed further in the companion article (Schripp et al., 2022). The ordinate values are the geometric mean discussed in the text.

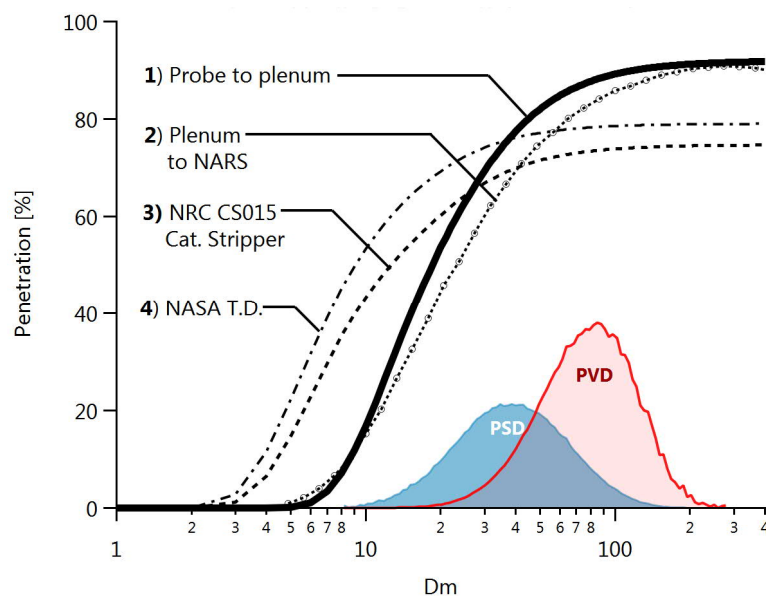


Figure 4. Penetration functions for the main probe-to-plenum sampling line as well as other components in the sampling system. Shaded areas illustrate a representative particle size (PSD) and volume (PVD) distribution measurement with GMD 34 nm and GSD 1.72. PSD data for all test points and instruments are provided in the supplement. NARS: North American Reference System; CS015: Catalytic Stripper; T.D.: thermodenuder.

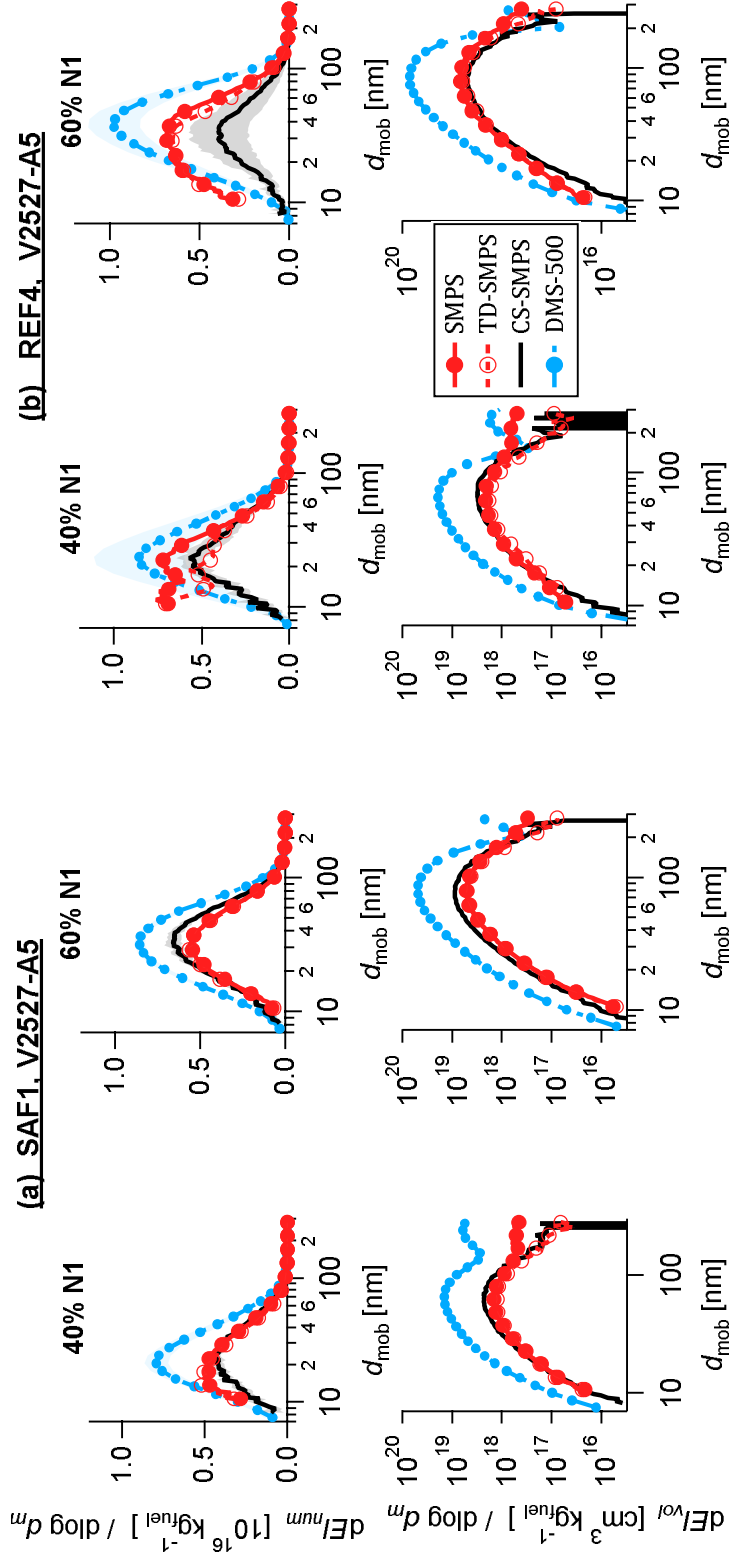
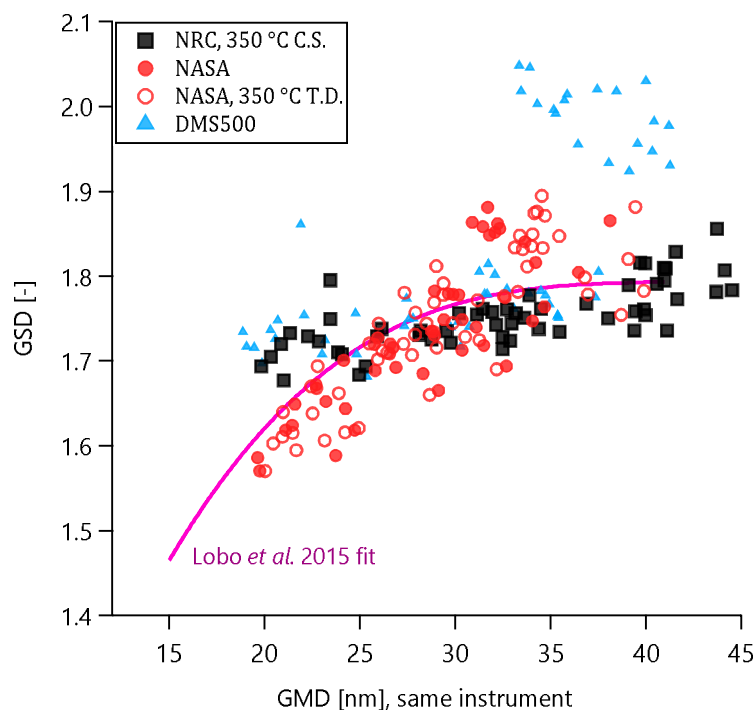


Figure 5. Selected PSDs illustrating the V2527-A5 engine with (a) SAF1 fuel and (b) REF4 fuel. Each panel shows 60% N1 on the right and a lower N1 on the left: 40% for (a), 60% for (b). Note that the TD-SMPS and CS-SMPS (red open circles and black line) represent nvPM, while the SMPS and DMS500 represent vPM.



1148

1149 Figure 6. GSD versus GMD data as by measured by each particle sizer for all test points.

1150 Higher GSDs for the DMS500 correspond to bimodal PSDs (non-volatile and volatile
 1151 modes). Note that size-dependent particle losses (see penetration functions in Figure 4)
 1152 may affect both GSD and GMD. Based on Figure 12, the TD-SMPS (NASA) data may be more
 1153 accurate than the CS-SMPS data (see text). Fit is from Lobo et al. (2015c).

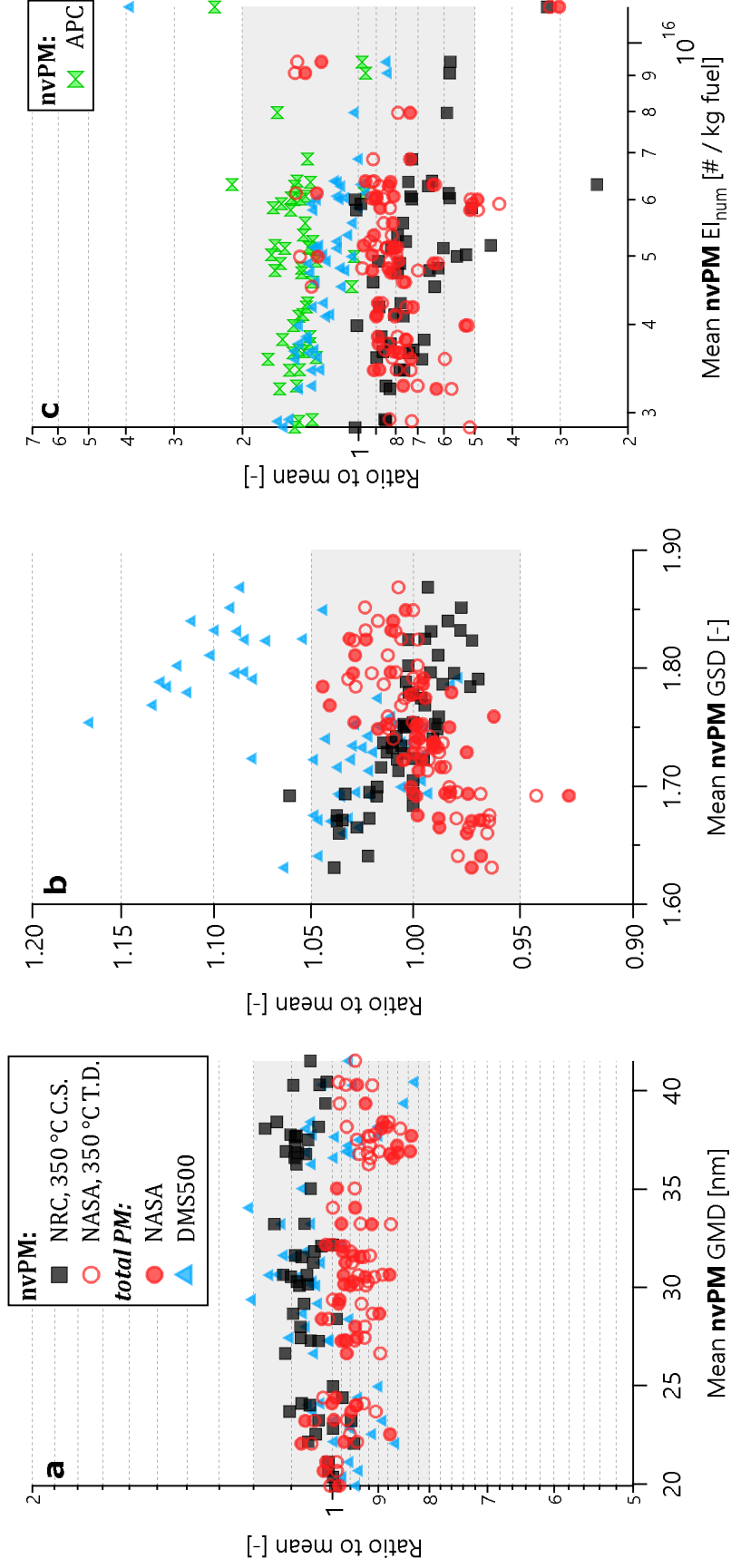


Figure 7. Comparison of size and number measurements in terms of GMD, GSD, and El_n . Grey shading shows 20%, 5%, and 200% in GMD, GSD, and El_n respectively. In panels (a) and (b), mean is defined from the CS-SMPS (NRC) and TD-SMPS (NASA) data. In panel (c), the mean additionally includes the APC (NARS) data (the APC is in the NARS and uses a TSI 3790E CPC).

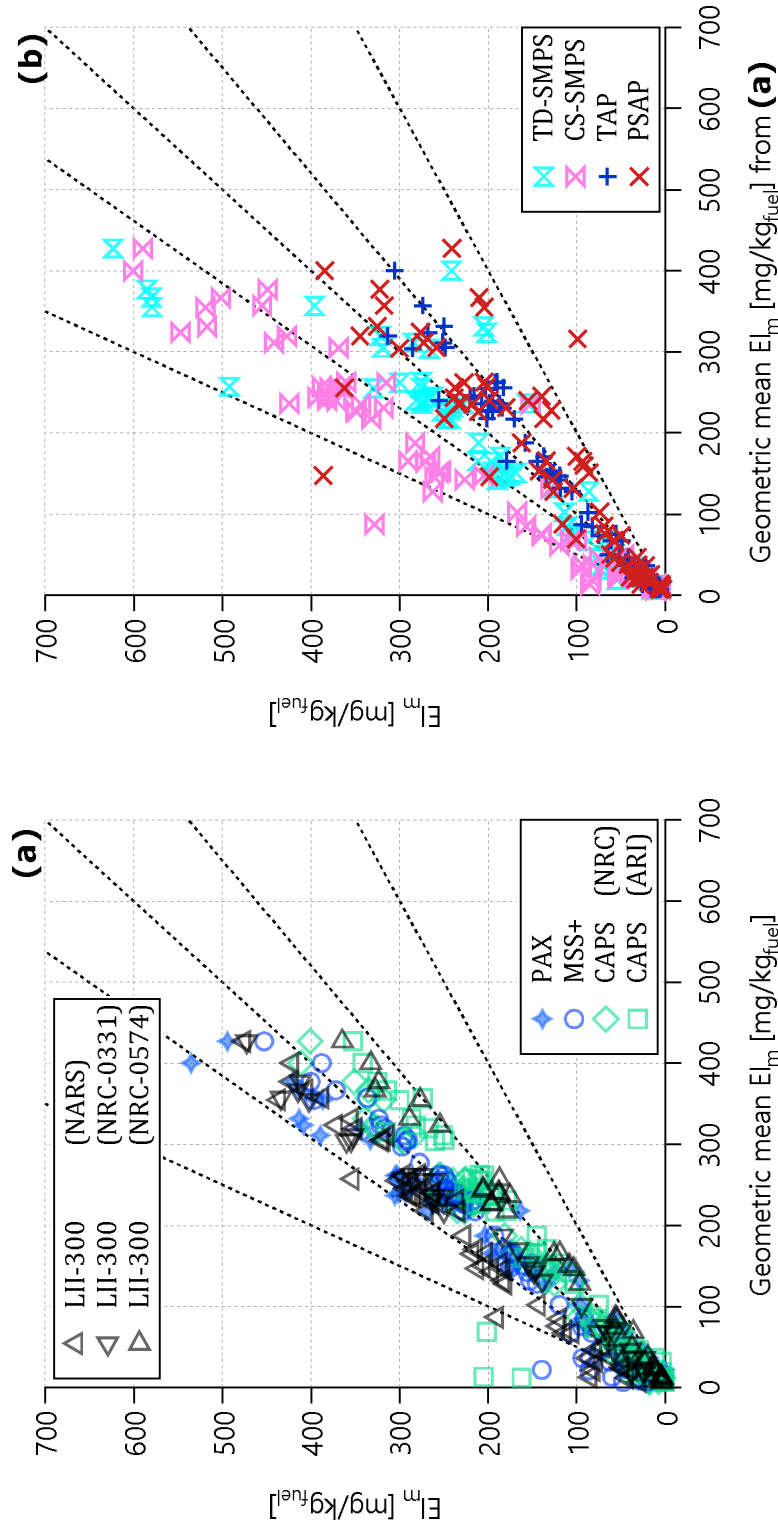


Figure 8. E_{I_m} scatterplot for (a) real-time and (b) integrative nVPM measurements. The term integrative refers to SMPS measurements (mass concentrations estimated by assuming unit-density spheres) and filter photometer measurements (mass concentrations estimated using standard empirical relationships between light attenuation and light absorption). The abscissa of both panels is the geometric mean of all available data from the 7 real-time sampling instruments plotted in (a). Angled lines illustrate slopes of 2, 2^{-1} , 1.3, 1.3^{-1} , and 1.0.

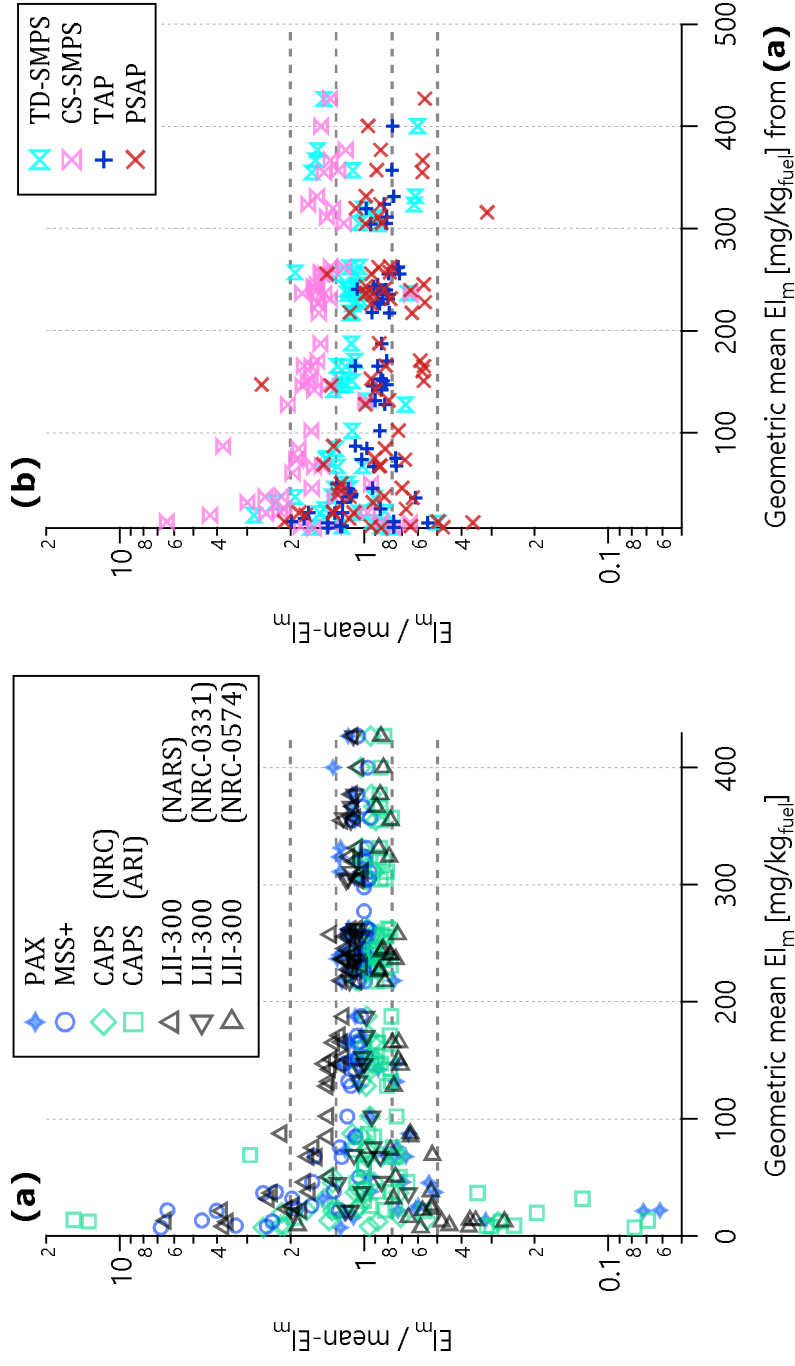


Figure 9. Ratio plots corresponding to Figure 8. The inner and outer horizontal lines show ratios of 2, 2⁻¹, 1.3, 1.3⁻¹, and 1.0. Agreement between the instruments is poorer at $El_m < 100$ mg/kg_{fuel}, which corresponds to an approximate concentration of $10 \mu\text{g m}^{-3}$ (the exact conversion factor varies with CO₂ concentration and fuel properties) and close to the limit of detection for most instruments.

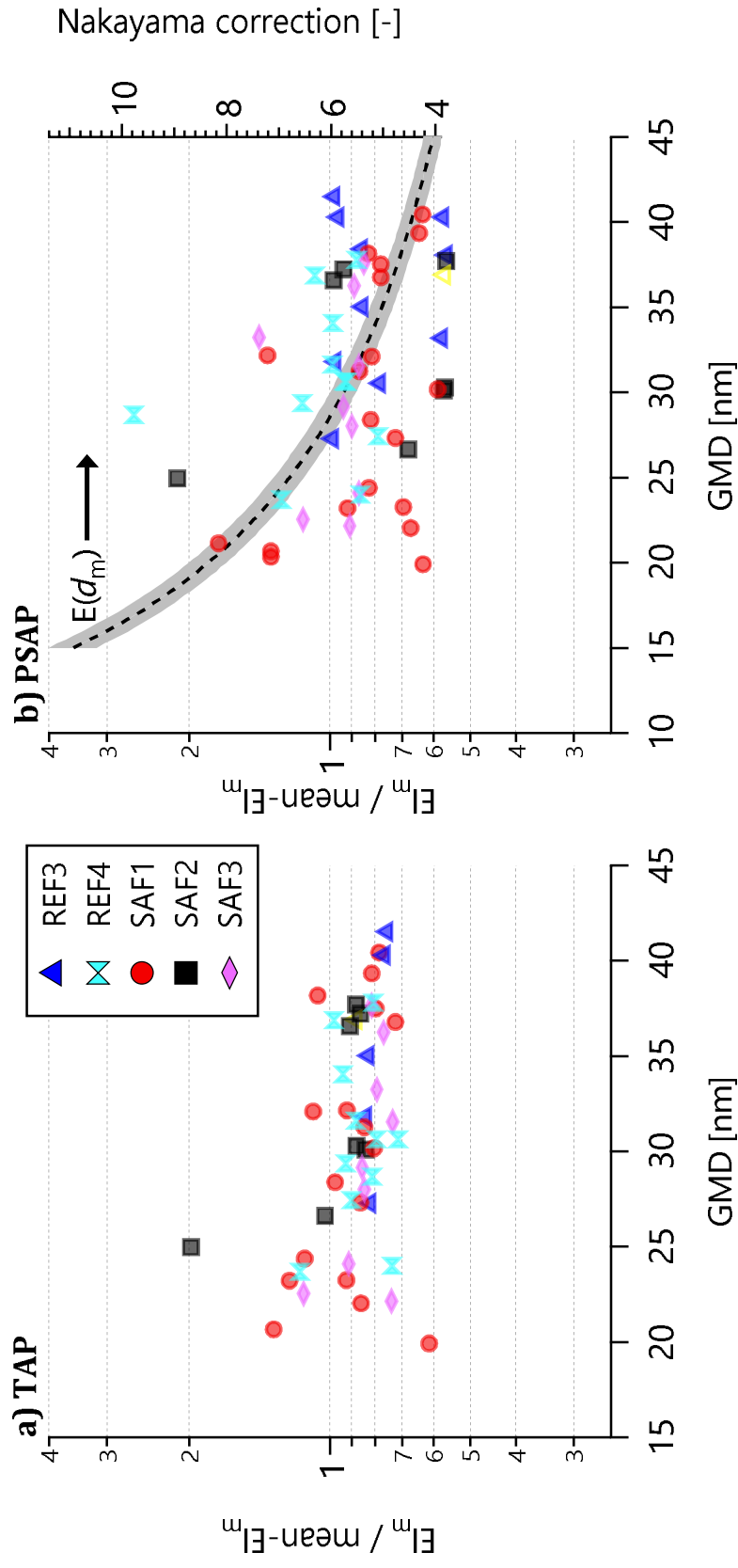
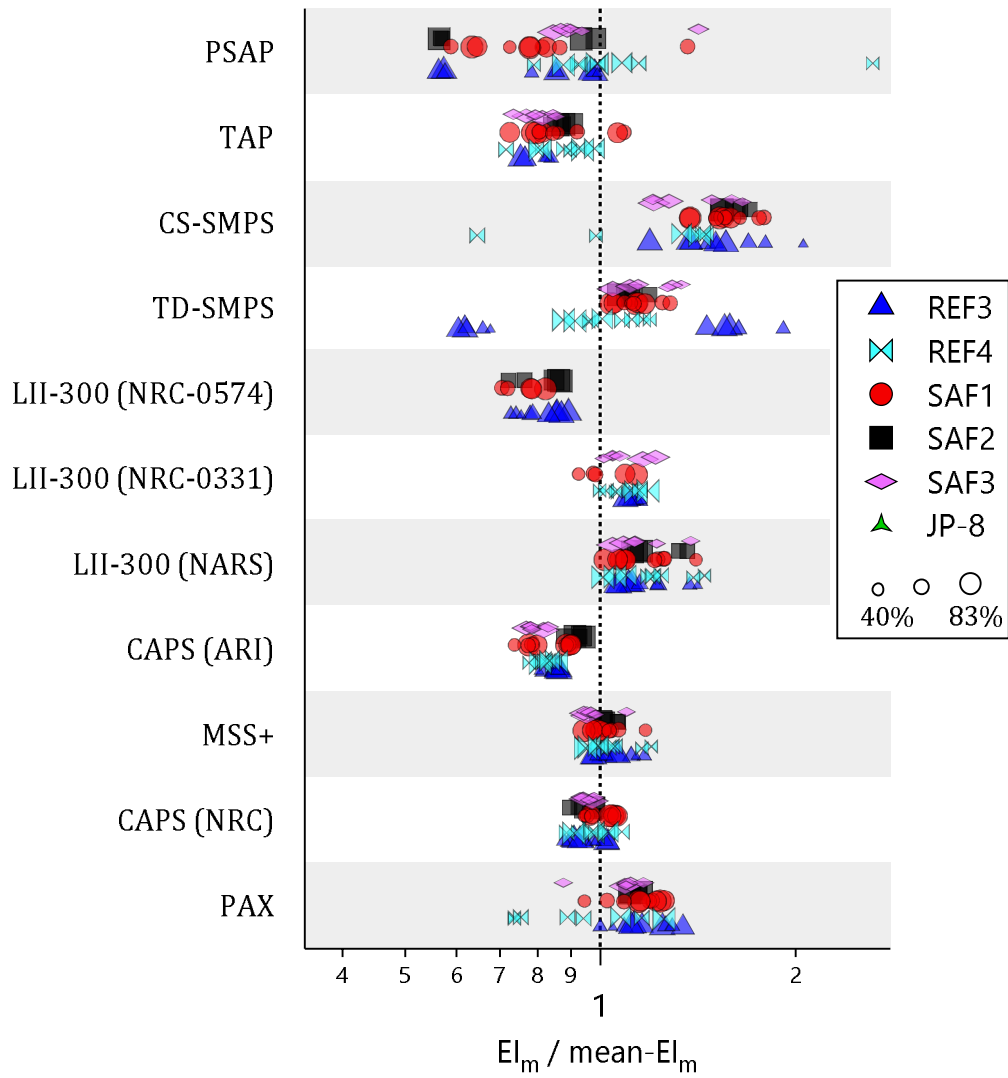
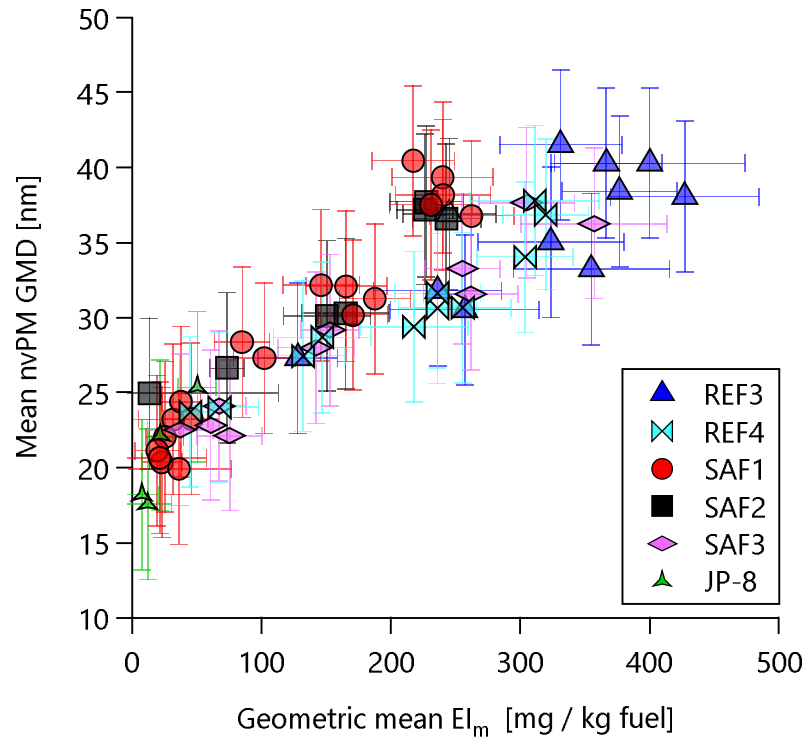


Figure 10. $EL_m / \text{mean-}EL_m$ ratios from Figure 9 for the TAP and PSAP (the filter-based photometers) only, plotted as a function of geometric mean mobility diameter (GMD) to highlight potential size-dependent sensitivities of these instruments. The curve labelled $E(d_m)$ in b) plots the size-dependent PSAP correction factor given by Nakayama et al. (2010; Eq. 8) with 1σ uncertainties shaded.



1172

1173 Figure 11. Ratios of Figure 9 grouped by fuel. All fuels except JP-8 were combusted in the
 1174 V2527-A5 engine; JP-8 was combusted in the CFM56-2C1 engine. Shading is to guide the
 1175 eye. Symbols are sized by N1 thrust. Plot excludes data where $EI_m < 25 \text{ mg/kg}_{\text{fuel}}$ and N1
 1176 thrust below 40% to minimize the effects of instrument noise and wind speed,
 1177 respectively, on the ratios.



1178

1179 Figure 12. Scatterplot of the mean nvPM GMD within test points against geometric
 1180 mean nvPM EI_m from Figure 8a. The correlation with GMD and EI_m indicates that Figure 9
 1181 implicitly represented different particle sizes.

1182

1183

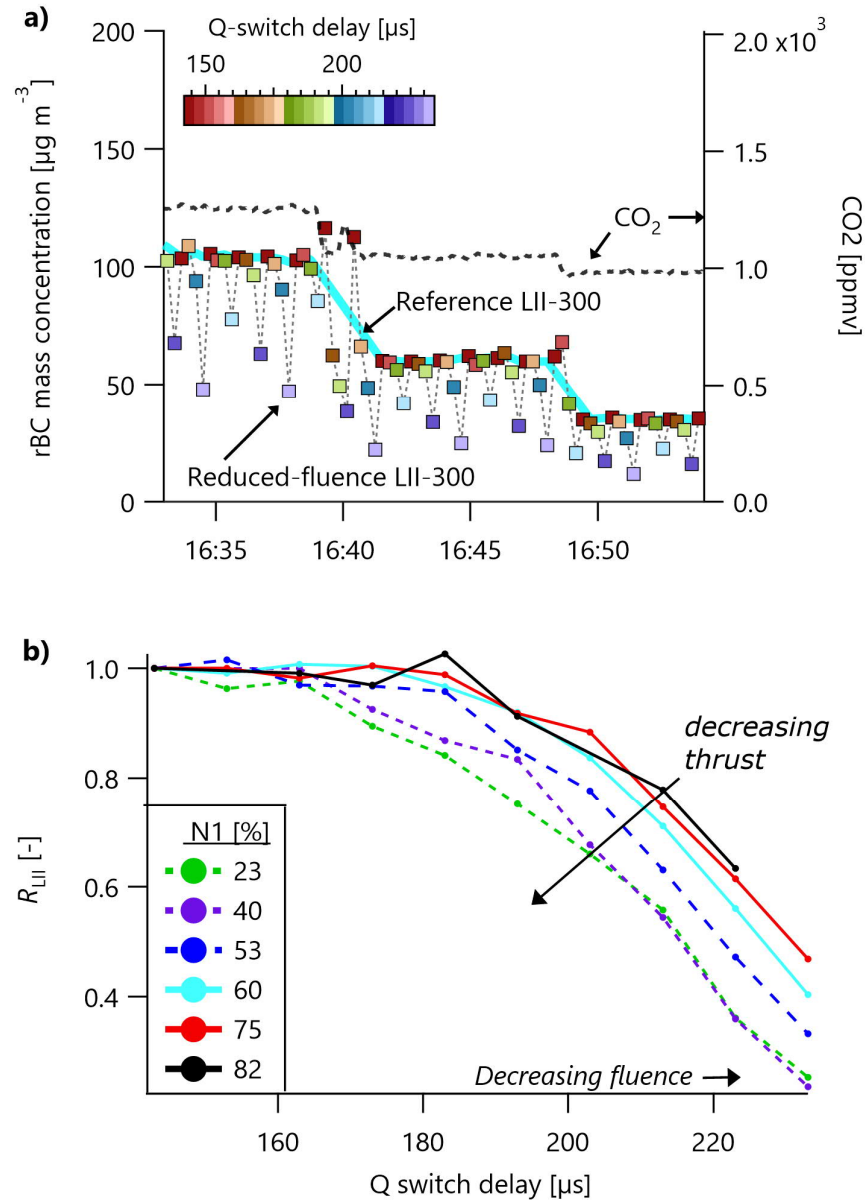


Figure 13. (a) LII 300 experiment time series, where one LII 300 was operated with increased Q-switch delays to reduce its laser fluence (squares) and the other was operated at standard fluence (solid line). CO_2 data are also shown for context. (b) The ratio R_{LII} of the concentration reported by the reduced-fluence LII divided by the reference LII. It is evident from (b) that the standard high-fluence conditions generate data that are independent of N1 thrust, and that moderate- and low-fluence conditions (Q-switch delays greater than about 165 to 185 μs) display a weak dependence on thrust.